Finanziato dall'Unione europea NextGenerationEU | Ministero dell'Università e della Ricerca | Italiadomani PIANO NAZIONALE DI RIPRESA E RESILIENZA

multi-Risk sciEnce for resilienT commUnities undeR a changiNgclimate

Codice progetto MUR: **PE00000005** – D43C22003030002

Deliverable title: Seamless modelling of water and sediment dynamics from nearshore circulation to inland flows and flows in transitional systems, with specific focus on swash zone dynamics and related interactions

Deliverable ID: 1.4.4

Due date: 30/05/2025

Submission date: 30/11/2023

AUTHORS

Giovanni Besio (UNIGE), Francesco De Leo (UNIGE), Andrea Margarita Lira Loarca (UNIGE), Agnese Baldoni (UNIVPM), Lorenzo Melito (UNIVPM), Daniele Trogu (UNICA), Sandro De Muro (UNICA), Marco Porta (UNICA), Andrea D'Alpaos (UNIPD), Alvise Finotello (UNIPD), Alice Puppin (UNIPD), Rosaria Musumeci (UNICT)

Technical references

Project Acronym	RETURN
Project Title	multi-Risk sciEnce for resilienT commUnities undeR a changiNg climate
Project Coordinator	Domenico Calcaterra UNIVERSITA DEGLI STUDI DI NAPOLI FEDERICO II domcalca@unina.it
Project Duration	December 2022 – November 2025 (36 months)

Deliverable No.	DV1.4.4
Dissemination level*	
Work Package	W1.P4 - Coastal flooding and beach erosion under environmental and climatic changes
Task	1.4.2 – Coastal floods and beach erosion hazard modelling
Lead beneficiary	UNIGE
Contributing beneficiary/ies	UNIGE, UNIPD, UNICA, UNIVPM, UNICT

* PU = Public

PP = Restricted to other programme participants (including the Commission Services)

RE = Restricted to a group specified by the consortium (including the Commission Services)

CO = Confidential, only for members of the consortium (including the Commission Services)

Document history

Version	Date	Lead contributor	Description
0.0	10/04/2024	Giovanni Besio	First Draft
1.0	27/04/2024	Andrea D'Alpaos, Alvise Finotello, Francesco De Leo, Agnese Baldoni, Lorenzo Melito, Daniele Trogu, Sandro De Muro, Alice Puppin, Marco Porta, Rosaria Musumeci	Work Draft
1.0	30/04/2024	Giovanni Besio	Release Draft

ABSTRACT

Numerical models are crucial for computing hydrodynamics in coastal environments as they offer a detailed and dynamic representation of complex physical processes. These models simulate the movement and interaction of water masses, taking into account factors such as tides, waves, currents, and sediment transport. By integrating real-world data and applying mathematical frameworks, numerical models help predict coastal behavior under various scenarios, including storm surges, erosion, and sea-level rise. This predictive capability is essential for coastal management, enabling the design of effective mitigation strategies, infrastructure planning, and environmental conservation. Ultimately, numerical models provide a robust tool for understanding and managing the delicate and dynamic nature of coastal systems, ensuring sustainable development and resilience against natural hazards.

The present document presents a review of the underlying equations for a number of well established models, along with studies and practical applications to selected case studies (i.e., Proof of Concepts), spread along the Italian coastlines.

Table of contents

Figures

1. Introduction

Numerous environmental processes occur in the nearshore zone, attracting significant attention from scientific and technical perspectives. These processes include storm surges (Enríquez et al., 2020), coastal circulation (Dagendorf et al., 2021), beach erosion (Oo et al., 2022), and pollutant dispersion (Li et al., 2022), among others1. Understanding nearshore climatology is therefore essential for managing human activities along coastal areas, as well as for hazard preparedness and response programs (Losada et al., 2019).

In this respect, numerical models play a crucial role in simulating and forecasting marine and coastal hydrodynamics, with advancements in supercomputing power driving their increased utilization. Through a modeling approach, indeed, it is possible to represent a physical system and how this will evolve to a change of its conditions. Numerical models aim to reproduce mathematically changes which describe a natural phenomenon, with lower costs compared with physical model experiments, and the opportunity to test several configurations with low effort. As such, various models have been developed to address geophysical fluid dynamics problems, including beach morphodynamics (Roelvink et al., 2010), littoral currents (De Goede, 2020), and ocean wave generation and propagation to the shallow waters (Rogers, 2020).

However, the models above usually rely on vast amounts of data, and in particular when climate reanalysis services with very high temporal and spatial resolutions, demanding significant computational resources, are employed. To tackle this issue, techniques aimed at reducing data dimensionality can be employed, allowing to focus on subsets thereby lessening computational burdens. In this framework, widely used tools are the clustering methods, which partitions input data into modes or clusters based on chosen distance measures, as to minimize intra-cluster distances while maximizing inter-cluster distances (Hennig et al., 2015). These clusters, often termed "scenarios," summarize the dataset's main properties, facilitating a prompt understanding of complex multi-variate datasets. Several clustering methods exist, each tailored to specific objectives. For instance, the K-means algorithm, a popular unsupervised clustering technique, has been widely used in environmental studies, though alternative methods may be preferred for certain data characteristics.

Cluster techniques have recently reached prominence among the oceanography and coastal engineering communities, and have been employed in a number of researches concerning e.g., the simulation of estuaries hydrodynamics (McLaughlin et al., 2003; Bárcena et al., 2015) the probability of marine litter accumulation, the propagation of ocean waves from the off-shore to the shallow waters (Camus et al., 2011b). In this report, the selection of relevant time-varying scenarios of meteocean parameters through clustering techniques is critically reviewed, and possible alternative approaches based on supervised classifications are proposed. The document is structured as follows. First, a review on nearshore circulation and other coastal processes is introduced, along with a description of different modeling approaches and related software (Sections 2 and 32). A general framework for the scenarios selection is presented in Section 4, while Section 5 presents three study cases. Finally, conclusions are drawn in Section 6.

[1] A few articles are reported in the Introduction for the sake of brevity; however, there are numerous researches that offer insights into the phenomena outlined.

2. Numerical Modelling of Physical Processes from the Offshore Region up to Swash Zone Dynamics

It is worth mentioning that, nowadays, most models and numerical codes have been validated for applications involving free-surface motions. There is indeed extensive documentation supporting the evidence that such models can adequately represent many physical processes in the field of environmental fluid mechanics. This Section presents the modeling approaches currently employed, depending on the researchers to be carried out.

2.1 Navier-Stokes Solvers (CFD)

CFD stands for Computational Fluid Dynamics, a numerical approach to examining fluid motion and the associated chemical-physical processes. Therefore, CFD indicates any numerical model used to model both turbulent and non-turbulent flows. However, in practice, the term mainly refers to codes capable of solving the full Navier-Stokes equations in all three dimensions, which read:

$$\frac{\partial u}{\partial x}+\frac{\partial v}{\partial y}+\frac{\partial w}{\partial z}=0$$

$$\frac{\partial u}{\partial t}+u\frac{\partial u}{\partial x}+v\frac{\partial u}{\partial y}+w\frac{\partial u}{\partial z}=-\frac{1}{\rho}\frac{\partial p}{\partial x}+\nu\nabla^2 u+F_x$$

$$\frac{\partial v}{\partial t}+u\frac{\partial v}{\partial x}+v\frac{\partial v}{\partial y}+w\frac{\partial v}{\partial z}=-\frac{1}{\rho}\frac{\partial p}{\partial y}+\nu\nabla^2 v+F_y$$

$$\frac{\partial w}{\partial t}+u\frac{\partial w}{\partial x}+v\frac{\partial w}{\partial y}+w\frac{\partial w}{\partial z}=-\frac{1}{\rho}\frac{\partial p}{\partial y}-g+\nu\nabla^2 w+F_z$$

(1)

Where u, v, and w are the velocity components along the x, y, and z directions; g is the gravity force, ν is the kinematic viscosity while F denote the source terms and ρ indicates the fluid density.

CFD refers to computationally complex computer simulations capable of handling various phenomena, ranging from aerodynamics to turbomachinery, coastal engineering, and biochemistry. CFD is a cutting-edge technique for industry and research applications; however, its high computational cost often limits its use. Historically, CFD was first used in the 1960s in the aerospace industry. However, the high computational cost of running CFD codes primarily restricted their use to research environments until the 1990s when computational resources began to become economically accessible. Since then, many CFD codes have been developed using a wide range of pre-processing, solving, and post-processing tools.

2.2 Hydrostatic models

Most numerical models used for ocean circulation and coastal studies solve the Reynolds-Averaged Navier-Stokes (RANS) equations. In fact, for intermediate to large scales, solving the full Navier-Stokes equations would be computationally undoable. Hence, a simplified version of RANS, known as the hydrostatic approximation, is usually employed. This means that the equation for vertical momentum is reduced to an approximation of hydrostatic equilibrium. Pressure is calculated based on the hydrostatic approximation, while the vertical component of velocity is determined using the continuity equation. In contrast, if the full Navier-

Stokes equations were considered, all velocity components would be directly calculated. Below are the RANS equations with the hydrostatic approximation:

$$\frac{\partial U}{\partial x}+\frac{\partial V}{\partial y}+\frac{\partial W}{\partial z}=0$$

$$\frac{\partial U}{\partial t}+U\frac{\partial U}{\partial x}+V\frac{\partial U}{\partial y}+W\frac{\partial U}{\partial z}=-g\frac{\partial h}{\partial x}+\nu_t\nabla^2U+F_x$$

$$\frac{\partial V}{\partial t}+U\frac{\partial V}{\partial x}+V\frac{\partial V}{\partial y}+W\frac{\partial V}{\partial z}=-g\frac{\partial h}{\partial y}+\nu_t\nabla^2V+F_y$$

$$P=P_{atm}+\rho_0 g(h-z)+\rho g\int_z^{Z_s}\frac{\Delta\rho}{\rho_0}dz' \qquad (2)$$

Where the capital letters indicate the average fluid velocity components.

2.3 Potential flow

Potential flow models assume that motion is irrotational and occurs at high Reynolds numbers, and are therefore mostly used to analyze external flows over solid surfaces. This type of model assumes the existence of a velocity potential function which satisfies the Laplace equation:

$$\nabla^2\Phi=0$$
(3)

Velocity components are obtained by differentiating the potential function Φ with respect to spatial coordinates. Since this type of model assumes an irrotational fluid motion, it is unable to describe phenomena such as the presence of the boundary layer or fluid-structure interaction.

2.4 Shallow Water Equations

When dealing with shallow water conditions, the motion is mainly horizontal, thus vertical accelerations can be deemed negligible. In such cases, the fluid dynamics are expressed via the so-called Shallow Water Equations, obtained by averaging the Navier-Stokes equations vertically:

$$\frac{\partial h}{\partial t}+\vec{\overline{U}}\cdot\nabla(h)+h\nabla\cdot\left(\vec{\overline{U}}\right)=0$$

$$\frac{\partial \overline{U}}{\partial t}+\vec{\overline{U}}\cdot\nabla\left(\overline{U}\right)=-g\frac{\partial h}{\partial x}+\frac{\tau_s+\tau_f}{\rho h}$$

$$\frac{\partial \overline{V}}{\partial t}+\vec{\overline{U}}\cdot\nabla\left(\overline{V}\right)=-g\frac{\partial h}{\partial y}+\frac{\tau_s+\tau_f}{\rho h}$$
(4)

Being τ_s and τ_f the bottom and surface frictions, respectively.

2.5 Boussinesq models

The propagation of waves over the intermediate depths (i.e., the region between shallow and deep waters) can be described by the Boussinesq model. This assumes that the fluid velocity is assumed to be constant throughout the water column, while the vertical component varies almost linearly. Such conditions are expressed as:

$$\frac{\partial \eta}{\partial t} + \frac{\partial}{\partial x}[(h+\eta)u_x] = 0$$

$$\frac{\partial u_x}{\partial t} + u_x\frac{\partial u_x}{\partial x} + g\frac{\partial \eta}{\partial x} = \frac{1}{2}\frac{\partial^3 (hu_x)}{\partial t\,\partial x^2} - \frac{1}{6}\frac{\partial^3 u_x}{\partial t\,\partial x^2}$$
(5)

Where u_x denotes the horizontal velocity averaged over the water column.

2.6 Spectral models

Spectral models are employed to describe ocean waves growth, propagation, and decay, by solving the action balance equation with no a priori restriction on the wave spectrum. Such models rely on the following equation:

$$\frac{\partial N}{\partial t} + \frac{\partial (c_x)N}{\partial x} + \frac{\partial (c_y N)}{\partial y} + \frac{\partial (c_\theta N)}{\partial \theta} + \frac{\partial (c_\sigma N)}{\partial \sigma} = \frac{S_{total}(x,y,t,\theta,\sigma)}{\sigma}$$
(6)

Where N is the wave action, defined as the spectral density over the wave frequency S is a source term while c denote the wave celerity components over the domain. These models rely on the spectral wave theory, assuming that a sea states can be described through a wave spectrum depending on waves frequency and direction (see Figure 1). More details about spectral wave models can be found in Booij et al., (2004) and WW3DG (2019).

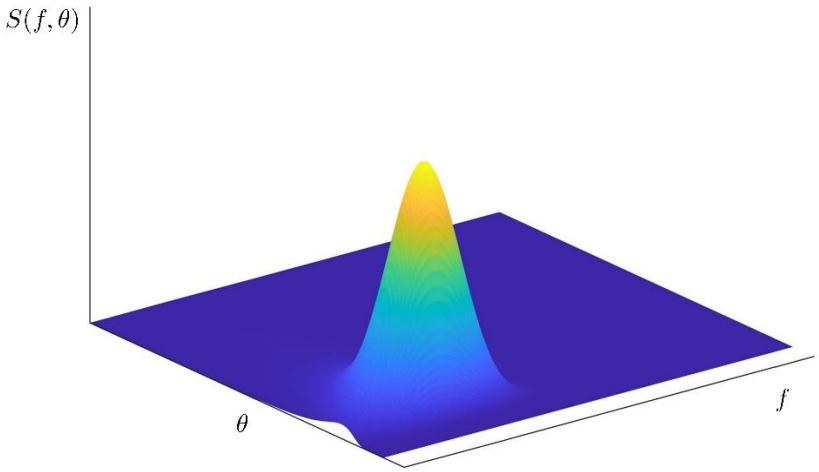

Figure 1. Example of a wave spectrum.

3. A hydro-morphodynamic model for shallow tidal basins

To reproduce sediment dynamics governing the morphodynamic evolution of shallow micro-tidal basins, a two-dimensional (2D) model is employed, that consists of three modules, namely the hydrodynamic module coupled with the wind-wave module (WWTM) (Carniello et al., 2011) and the sediment transport and bed evolution module (STABEM) (Carniello et al., 2012).

The hydrodynamic module solves the 2D depth-integrated shallow water equations (SWEs), phase-averaged over a representative elementary area of irregular topography to deal with very shallow flows, wetting, and drying (Defina, 2000). Projected on a Cartesian frame (x, y), the SWEs read:

$$\vartheta(\eta)\frac{\partial \eta}{\partial t} + \nabla \cdot \mathbf{q} = 0 \tag{7}$$

$$\frac{\mathrm{D}}{\mathrm{D}t}\left(\frac{\mathbf{q}}{Y}\right) + \frac{1}{Y}\nabla \cdot \mathbf{Re} + \frac{\boldsymbol{\tau}_t}{Y\rho} - \frac{\boldsymbol{\tau}_s}{Y\rho} + g\nabla h = 0 \tag{8}$$

where t is time, η is is the free surface elevation over a datum, $\mathbf{q} = (q_x, q_y)$ is the depth-integrated velocity (i.e., discharge per unit width), ∇ and $\nabla \cdot$ denote the 2D gradient and divergence operators. The term ϑ is the wet fraction of the computational domain that depends on the water depth and on the local topographic unevenness (Defina, 2000). In the momentum eq. (8), $\mathrm{D}/\mathrm{D}t$ is the material (or Lagrangian) time derivative, Y is the water volume per unit area (i.e., the equivalent water depth), $\boldsymbol{\tau}_t$ and $\boldsymbol{\tau}_s$ are the shear stresses at the bottom (due to tidal currents) and at the free surface (due to wind drag), respectively, ρ is the water density, and g is gravity. The Reynolds stresses are computed using a depth-averaged version of Smagorinsky's model (Smagorinsky, 1963). In tensor index notation, they read:

$$\mathbf{Re} = R_{ij} = \nu_e Y\left(u_{i,j} + u_{j,i}\right) \tag{9}$$

$$\nu_e = 2C_S^2 A_e \sqrt{2\left(u_{x,x}\right)^2 + \left(u_{x,y} + u_{y,x}\right)^2 + 2\left(u_{y,y}\right)^2} \tag{10}$$

with i, j in eq. (9) denoting either the x or y coordinates and $\mathbf{u} = \mathbf{q}/Y$. The eddy viscosity, ν_e, is proportional to the strain rate, with A_e the area of the computational element and $C_s = 0.2$ the Smagorinsky coefficient.

In the numerical scheme, the material derivative in (8) is expressed as the finite difference in time and solved with the method of characteristics. This mixed Eulerian-Lagrangian approach allows solving the continuity equation (7) with a semi-implicit scheme, which leads to a self-adjoint spatial operator. It is solved on a staggered triangular grid with the finite element method of Galerkin (Defina, 2000) and flow rates are obtained by back-substitution.

The wind-wave module (Carniello et al., 2011) solves the wave action conservation equation using the same computational grid of the hydrodynamic module, that provides water depths and depth-averaged flow velocities, used to propagate the wind-wave field. The wave action density (N_0) in the frequency domain evolves according to (Carniello et al., 2011):

$$\frac{\partial N_0}{\partial t} + \frac{\partial}{\partial x}c'_{gx}N_0 + \frac{\partial}{\partial y}c'_{gy}N_0 = S_0 \tag{11}$$

where c'_{gx} and c'_{gy} are the group celerity components of wave used to approximate the propagation speed of N_0 (Carniello et al., 2011; Holthuijsen et al., 1989). The wind-wave source terms, grouped in the term S_0, account for positive (wind energy input) and negative (bottom friction, whitecapping and depth-induced breaking) contributions to wave energy. The model computes the spatial and temporal distribution of the wave periods based on the relationship between peak-wave period, local wind speed, and water depth (Young &

Verhagen, 1996). As the lagoon margins are almost vertical and jagged, refraction is neglected and waves are assumed to propagate in the wind direction. The horizontal orbital velocity at the bottom, which is obtained from the significant wave height through the linear wave theory, provide the additional component of the bottom shear stress, τ_w, induced by the wind-wave field. The nonlinear interactions between τ_w and the current-induced bottom shear stress (τ_t) are accounted for by means of the empirical formulation by Soulsby (Soulsby, 1995), which increases the value of the total bottom shear stress, τ_b, beyond the mere sum of τ_t and τ_w.

Using the same computational grid, the STABEM module (Carniello et al., 2012) solves the advection-diffusion equation for suspended sediment with a conservative, second-order in space scheme and the Exner's equation:

$$\frac{\partial C_i Y}{\partial t} + \nabla \cdot (\boldsymbol{q} C_i) - \nabla \cdot (\mathbf{D}_h \nabla C_i) = E_i - D_i \qquad i = s, m \tag{12}$$

$$(1-n)\frac{\partial z_b}{\partial t} = \sum_i (D_i - E_i) \tag{13}$$

where C is the depth-averaged sediment concentration, $\mathbf{D}_h(x, y, t)$ is space- and time-dependent two-dimensional diffusivity tensor, assumed equal to the eddy viscosity computed by the hydrodynamic module (Viero & Defina, 2016), E and D represent the entrainment and deposition of bed sediment, z_b is the bed elevation and n the bed porosity, assumed equal to 0.4. The subscript i refers to the non-cohesive (sand, s) and cohesive (mud, m) sediment classes that typically characterize the bed of tidal lagoons. The relative content of mud (p_m), which represents the sum of clay and silt, is assumed to vary both in time and space; it determines the cohesive or non-cohesive behaviour of the mixture and the critical value of the bottom shear stress. The threshold value of mud content $p_{mc} = 10\%$ is assumed to discriminate between non-cohesive and cohesive behavior (Van Ledden et al., 2004). Based on measurements in the Venice Lagoon, the median diameters D_{50} adopted in the simulations to describe cohesive and non-cohesive sediments are 20 μm and 200 μm, respectively (Carniello et al., 2012).

The deposition rate of sand D_s is computed as

$$D_s = w_s r_0 C_s \tag{14}$$

where w_s is the absolute value of the sand settling velocity and r_0 is the ratio of near-bed to depth-averaged concentration which is here assumed constant and equal to 1.4 (Parker et al., 1987)

The deposition rate of pure cohesive mud, D_m, is given by Krone's formula:

$$D_m = w_m C_m \max\{0; 1 - \tau_b/\tau_d\} \tag{15}$$

where w_m is the absolute value of the mud settling velocity, τ_b the bottom shear stress computed by the hydrodynamic module, and τ_d the critical shear stress for deposition ($\tau_d = 1.0\ Pa$). The settling velocities, w_s and w_m, are computed using the Van Rijn formulation (van Rijn, 1984) for solitary particles in clear and still water, thus not incorporating flocculation effects which are negligible for particle diameter larger than 20 μm (Mehta et al., 1989).

The erosion rate strongly depends on the degree of cohesion of the mixture. For non-cohesive mixtures ($p_m < p_{mc}$), the erosion rate of sand, E_s, is described by the Van Rijn formulation (van Rijn, 1984), whereas the erosion rate of mud, E_m, can be computed through the formulation proposed by Van Ledden (Van Ledden et al., 2004) as follows:

$$E_s = (1-p_m)w_s \cdot 1.5 \left(\frac{D_{50}/Y}{D_*^{0.3}}\right) T^{1.5} \qquad for\ p_m < p_{mc}$$
$$E_m = \frac{p_m}{1-p_m} M_{nc} T \tag{16}$$

For cohesive mixtures ($p_m > p_{mc}$), both sand and mud erosion rates can be computed using the Partheniades's formula

$$E_s = (1-p_m) \cdot M_c\, T \qquad for\ p_m > p_{mc}$$
$$E_m = p_m \cdot M_c\, T \tag{17}$$

In equations (16) and (18), D_* is the dimensionless grain size ($D_* = D_{50}[(s-1)g/\nu^2]^{1/3}$, being s the sediment specific density and ν the water kinematic viscosity), T is the transport parameter, M_{nc} and M_c are the specific entrainment for non-cohesive and cohesive mixtures respectively (Van Ledden et al., 2004; van Rijn, 1984)

$$M_{nc} = \alpha \frac{\sqrt{(s-1)gD_{50}}}{D_*^{0.9}}, \qquad M_c = \left(\frac{M_{nc}}{M_m} \cdot \frac{1}{1-p_{mc}}\right)^{\frac{1-p_m}{1-p_{mc}}} \cdot M_m \tag{18}$$

where M_m is the specific entrainment for pure mud ($M_m = 5 \cdot 10^{-2} g\ m/s$) and α is set equal to $1 \cdot 10^{-5}$.

The transport parameter is usually defined as $T = \max\{0; \tau_b/\tau_c - 1\}$, describing a sharp transition between $T = 0$ and $T = \tau_b/\tau_c - 1$, where τ_b is the local bottom shear stress and τ_c is the critical shear stress for erosion. However, in real tidal systems, both τ_b and τ_c are not constant in space, thus we assume that they are both random variables, following a log-normal distribution (Carniello et al., 2012). The result of this stochastic approach is a smooth transition between $T = 0$ and $T = \tau_b/\tau_c - 1$.

All parameters are within the range of variability of similar deposition and erosion formulations (Breda et al., 2021; Temmerman et al., 2005). In particular, erosion is set equal to zero on salt marshes because vegetation reduces velocity and dampens waves, protecting sediment from erosion (Möller et al., 1999; Temmerman et al., 2005)

The result of erosion and deposition fluxes of sand and mud is a variation in bed level through time, which is computed according to eq. (13).

The model has been widely benchmarked against hydrodynamic, wind-wave, and turbidity field- and satellite data from the Venice Lagoon (Italy) (Carniello et al., 2011, 2014), Virginia Coast Reserve lagoons (USA) (Mariotti et al., 2010), and Cadiz Bay (Spain) (Zarzuelo et al., 2018).

4. Clustering methods for the selection of meteocean scenarios

The most common clustering methods can be grouped in two families, namely partitional techniques and hierarchical methods; the differences between the two is beyond the scope of the present report, thus interested readers are referred to Reddy & Vinzamuri (2018). The vast majority of past research concerning coastal engineering and oceanography applications took advantage of partitional techniques, for which a common work-flow can be established.

Let consider a dataset consisting of a number V of variables, each populated by n elements. Following the flowchart proposed in Camus et al., (2011), the first step to cluster such a dataset is to reshape it into a matrix, normalizing the elements into a common space and on a per-column base.

$$X_{n,V} = \begin{bmatrix} x_{1,1} & \dots & x_{1,V} \\ \vdots & \ddots & \vdots \\ x_{n,1} & \dots & x_{n,V} \end{bmatrix} \tag{19}$$

Each column vector of the matrix represents a variable of the dataset properly normalized, for example, by centering the data around the mean and then scaling it by the standard deviation, as shown below:

$$X'_{:,j} = \frac{x'_{:,j} - \mu\left(x'_{:,j}\right)}{\sigma\left(x'_{:,j}\right)} \tag{20}$$

Where μ and σ represent, respectively, the mean and the standard deviation of the j-th column of the matrix $X_{n,V}$. This operation is necessary as it allows the clustering algorithm to handle both negative and positive data, characterized by different orders of magnitude, preventing those spanning higher values from affecting all subsequent calculations (clustering is indeed based on the Euclidean distance, as explained further on in the text).

The scheme above leads to the selection of data associated to single time steps. By contrast, if scenarios varying through time are sought, it is first necessary to reshape the initial time series. After selecting a number nt of time instants, the individual vector x of a given variable is modeled in a matrix form as follows:

$$x'_j = x[i\delta + 1 : nt + i\delta], i = 0, \dots, \frac{n - nt}{\delta}\ ; j = i + 1 \tag{21}$$

Where δ represents the shift between two subsequent time instants (i.e., the number of time steps between the initial instants of two consecutive subsets x'). The clustering is then performed on the resulting matrix X', where each row defines a window of length nt for a given variable. Equation (22) summarizes the procedures introduced earlier.

$$X = \begin{bmatrix} x_1 \\ x_2 \\ \vdots \\ x_{nt} \\ \vdots \\ x_n \end{bmatrix} \qquad X' = \begin{bmatrix} x_1 & \cdots & x_{nt} \\ x_{i\delta+1} & \cdots & x_{nt+i\delta} \\ \vdots & \cdots & \vdots \\ x_{n-nt+1} & \cdots & x_n \end{bmatrix} \tag{22}$$

When working with multiple parameters, the steps outlined above should replicate for each of them, concatenating the resulting matrices into a matrix of total dimensions *[n-nt+1]* × *[nt x V]*. The rows of the final matrix are then grouped among different clusters represented by as many centroids, that allow to describe most of the data variability through a reduced number of elements.

Among the partitional methods, two common approaches are the K-Means and the Maximum Dissimilarity Algorithm. While the former extracts centroids describing the mean of the point cloud in the respective clusters, the latter yields elements along their boundaries (see the example in Figure 2). Thorough details about the methods can be found e.g. in Camus et al, (2011).

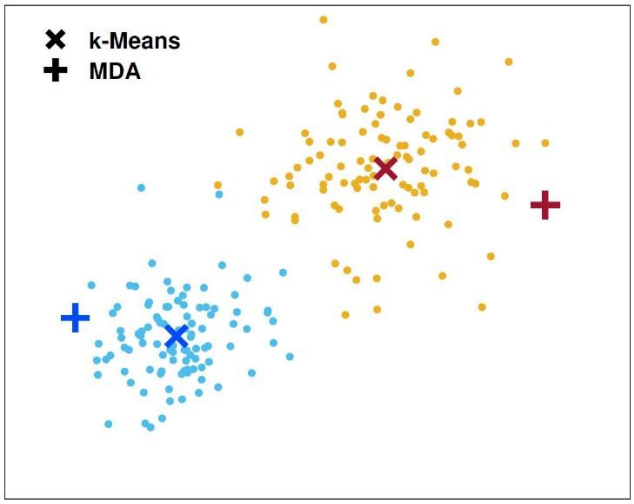

Figure 2. Example of partitional methods applied to a 2D dataset made of two subsets highlighted by different colors. Centroids resulting from k-means and MDA are indicated with different markers, as shown in the legend.

5. Proof of Concept Study Cases

5.1 Genoa Sturla

Sturla is one of the main beaches within the urban area of Genoa (Ligura, Italy). It is located in the eastern part of the city and is widely exploited by the local community for both recreational uses and commercial activities. However, through the past recent years, it has experienced severe flooding and erosion due to the increasing frequency of the sea storms and since the coast is fully exposed to the major fetches triggering waves. As such, it is crucial to characterize the coastal dynamics, as to support efficient policies and projects design.

Figure 3. The beach of Sturla to the east of the Genoa's Port.

In this framework, a numerical modeling of coastal hydro-dynamics is proposed, through the use of the numerical model X-Beach. This is capable of computing nearshore hydrodynamics and the morphodynamical response during storm-events, such as dune erosion, overwash and scour around buildings by solving the shallow water equations (see Section 2). The model was set-up in the area of interest (see the yellow box in Figure 3), leveraging a staggered variable-pitch type grid, with a spatial resolution varying from 10 m at the boundaries up to 3 m close to the coast.

The model is forced with wave stressors, taking advantage of the hindcast data reconstructed by the Department of Civil, Chemical, and Environmental Engineering (DICCA; http://www3.dicca.unige.it/meteocean/hindcast.html). The hindcast is defined over the entire Mediterranean Sea with variable resolution spanning from ≈25 km offshore to ≈300 m to the coast, and covers the 1979-2023

period at a hourly resolution and provides the main wave parameters, such as spectral height (H_s), mean and peak period (T_m and T_p, respectively) and directions (θ_m and θ_p, respectively).

The geometry of the coastline is defined through the data of Regione Liguria (https://geoportal.regione.liguria.it/), while the bathymetry is interpolated at the grid nodes based on local surveys carried out with low-cost sonar devices (https://v1.deepersonar.com/it/it_it/prodotti/smart-sonar-chirp-plus-2) and single-beam campaigns.

To select the most relevant sea states in the area, hindcast data are first reorganized according to Sect. 4; next, different clustering techniques are tested, i.e., K-Means, DBscan, and Maximum Dissimilarity Algorithm (MDA) to select the centroids of the resulting clusters, which are finally retained as significant scenarios. Figure 4 shows an example of such data selection.

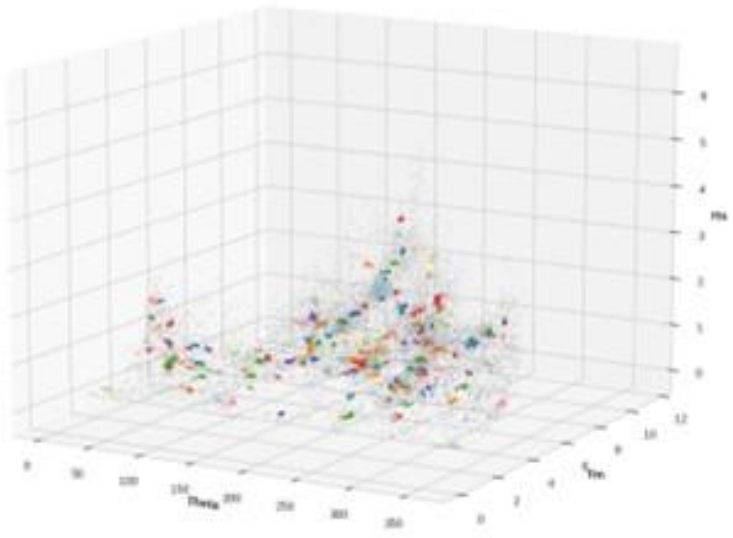

Figure 4. Centroids selected according to the DBScan method applied to H_s, T_p, and θ_p.

All scenarios selected through the clustering analysis consists of unique combination of spectral wave parameters, which are next used to feed the shallow water equations and solve the free surface flow by X-Beach. For the sake of brevity, further on in the paper a single case is presented, as detailed below:

Table 1. Wave parameters associated to a single scenario used to force the X-Beach model.

Fetch	**H_s [m]**	**T_p [s]**	**Θ_p [°N]**
Libeccio	2.61	6.77	203

The following figures show the results of the simulation, both as regards the littoral currents triggered by the wave motion (Figure 5) and the free surface elevation. These data can be next used for assessing littoral sand transport (and thus beach erosion and accretion) and flooding hazard due to wave induced Run-Up (Figure 6).

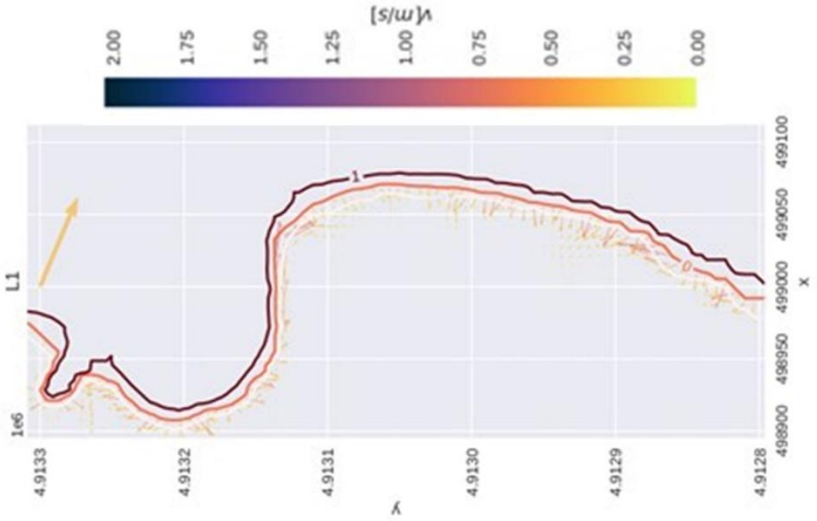

Figure 5. Current velocities induced in the proximity of the shoreline.

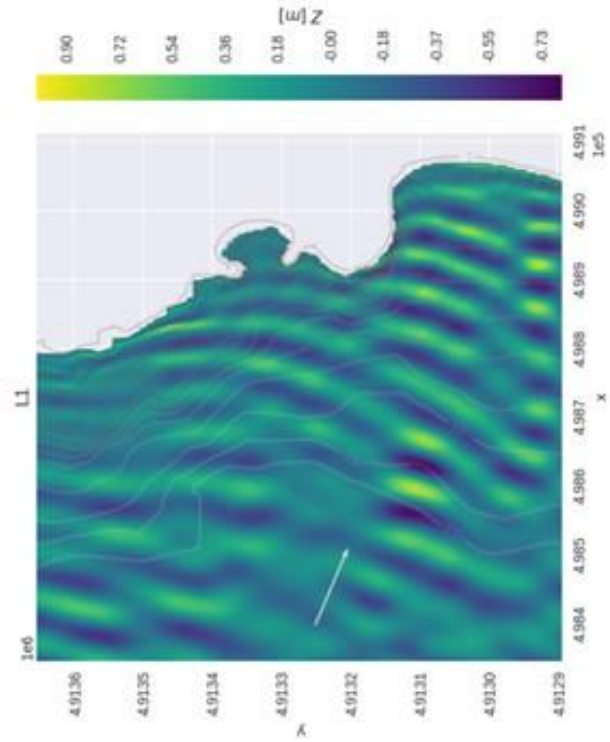

Figure 6. Water level elevation in the area.

5.2 Misa River Estuary

The Misa River Estuary (MRE, Senigallia, Italy) hosts an integrated monitoring system, deployed since 2015 within the EsCoSed and MORSE projects, two collaborative efforts between the Università Politecnica delle Marche (UNIVPM, Ancona, Italy) and the US Naval Research Laboratory (NRL, Stennis Space Center, MS). The existing instrumentation has been collecting data for more than six years and has been providing a large amount of real-time environmental information. This, coupled with the fact that the river is highly engineered in its final stretch flowing across the urban area, makes the site a field-scale laboratory for the study of nearshore and estuarine processes. In particular, the interaction between marine and river forcing can be observed and analysed.

The monitoring infrastructure (Figure 7) is characterized by two remote sensor systems, i.e. the SGS video-monitoring station, equipped with four cameras recording the final Misa River (MR) reach, the estuary and the nearshore area (blue pin), and an X-band radar, which is able to collect data for the reconstruction of wave field and bathymetry (up to 6 km from the shore; red pin). Onsite sensors are also installed: an offshore ADCP, which collects the offshore wave characteristics (yellow pin); a tide gauge, which gather the water surface elevation in the Senigallia harbour (cyan pin); a stream gauge, collecting the water surface level and discharges in the MR, about 1 km upriver of the mouth (green pin). The whole instrumentation provides data that is continuously stored in a dedicated server.

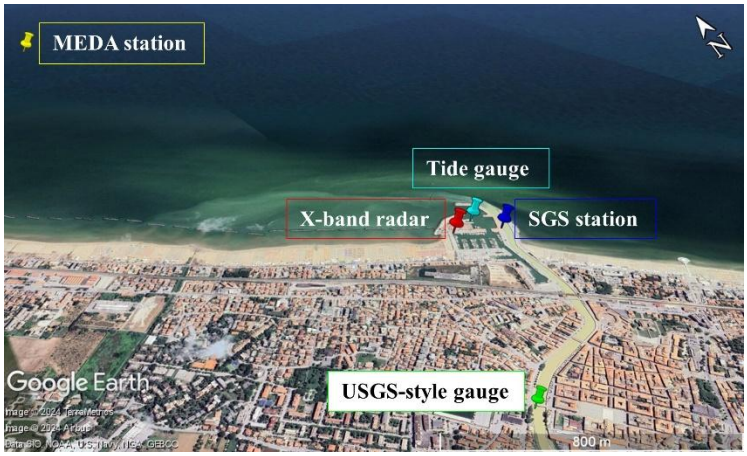

Figure 7. Instrumentation installed within and nearby the MRE.

Within the MARCUS project, two types of instruments will be installed to gain knowledge about sediment transport. Two probes and two sediment traps, like the one shown in Figure 8, will be deployed on the riverbanks to measure suspended and bedload transport, respectively. Aqua TROLL 600 is a multiparameter sonde that will acquire data of water level and turbidity. Sediment traps will be deployed, one facing the sea and one facing upstream, to quantify the sediment transport in both directions.

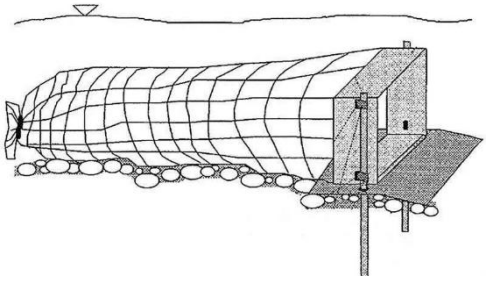

Figure 8. Example of sediment trap.

The MR flows within a small-scale basin (383 km^2) characterized by a torrential regime and large sediment transport. Like other Apennine Mountains rivers, although relatively small in size, it distributes large quantities of sediment, generated by the easy erosion of the rocks that constitute the Apennines. The suspended sediment discharge from the MR is estimated to be between 4.7· 10^8 kg/yr and 8.4· 10^8 kg/yr (Milliman and Syvitski, 1992; Frignani et al., 2005). The sediment grain sizes throughout the MR can range from clay to cobble. The riverbed surface is mainly composed of silt and clays (mainly montmorillonite minerals), with thick layers of muddy sediments and with percentage of sand and gravel increasing while approaching the river mouth (Brocchini et al., 2017). This was also confirmed by in situ samplings (Consorzio di Bonifica delle Marche, 2020), carried out in 2019, showing that cohesive materials dominate the riverbed composition in the upper stretch of the MR, while the amount of sand and gravel increases towards the mouth. Such riverbed composition is strongly affected by the environmental conditions and changes very dynamically.

The coast of Senigallia is characterized by a very mildly sloping sandy beach, defended by breakwaters to the North of the MR estuary, while part of a natural open coast to the South. The coastline has a NW–SE orientation and faces approximately 40° from the North. The beach is characterized by medium (D_{50}=0.25−0.5mm) to fine (D_{50}=0.125−0.25mm) sand in its emerged portion and by fine sand in its submerged profile, with the sediment size decreasing moving toward the South (Postacchini et al., 2017). The coast of Senigallia is located in a micro-tidal environment, with maximum tidal excursion rarely exceeding 0.6 m (Mohamed et al., 2019)[2]. The wave climate is characterized by two main wave regimes, induced by dominant and prevailing winds blowing on the Adriatic Sea, namely, Bora and Levante-Scirocco. The Bora is a cold NNE wind with a relatively short fetch since it flows along the minor axis of the narrow and elongated Adriatic basin. It generates short, steep and high waves that propagate almost perpendicular to the coast. On the contrary, the Levante-Scirocco is a warm wind that blows from ESE along the major axis of the Adriatic Sea, this resulting in a longer fetch and long and less steep waves coming from ESE. These waves are typically associated with a large storm surge. Both NNE and E waves can enter the river channel, but since the final stretch of the MR faces approximately 30° from the North, NNE waves penetrate more easily than E waves.

Several processes occurring at the MRE site have been studied through field observations, numerical modeling or a combination of both. The following sections describe some works on sediment transport at the MRE and surrounding beaches.

A description of the modeling chain used to simulate the propagation of waves from offshore to the shoreline is described in the final section.

[2] HOMEPAGE (mareografico.it)

5.2.1 Sandbars evolution

Predominantly sandy beaches in wave-dominated coasts, such as the Senigallia coastline, frequently feature submerged sand bars, i.e. local reliefs of the sea bottom that are generated as a result of the complex patterns of sediment transport generated by the hydrodynamic processes evolving in the surf zone. Sand bars are crucial for the self-protection of sandy coasts, since they serve as preferential points of wave energy dissipation through breaking: therefore, they are effective in reducing the overall amount of wave energy reaching the shoreline and the emerged beach. As a consequence of this, submerged sand bars have relevant implications on a number of aspects pertaining to coastal protection, as they influence coast stability in both short and long terms, beach erosion, and ensuing shoreline changes.
Studying the evolution of sand bars is fairly complex due to the number of hydrodynamic and morphological variables involved. It is generally well understood that sand bars are not static features of the coastline; on the other hand, they continuously adapt to the surrounding wave conditions. In the short term, bars tend to migrate offshore under moderate and intense wave climate, mainly thanks to strong offshore-directed currents developing under breaking waves, which are effective in redistributing sand bar sediment seaward. Onshore bar motion is, conversely, generally promoted by milder wave climates.

A study of sand bars features and migration patterns in response to wave climate has been proposed for the mildly sloped coast of Senigallia (Melito et al., 2020). The peculiar presence of a heavily engineered river mouth close to the unprotected beach is an opportunity to investigate the behavior of sand bar groups in two distinct environmental settings: (1) along a stretch of free, unprotected, dominantly long-shore uniform coast, with no influence of breakwaters and surrounding concrete structures (named Senigallia in the study), and (2) in a portion of beach that is artifically embayed by the presence of one of the concrete jetties delimiting the Misa river mouth (named Senigallia Estuary in the study). Sand bar analysis has been also performed for the comparatively steeper beach of Terracina (Lazio, Italy) for intra-site comparison of bar features and patterns (Figure 9).

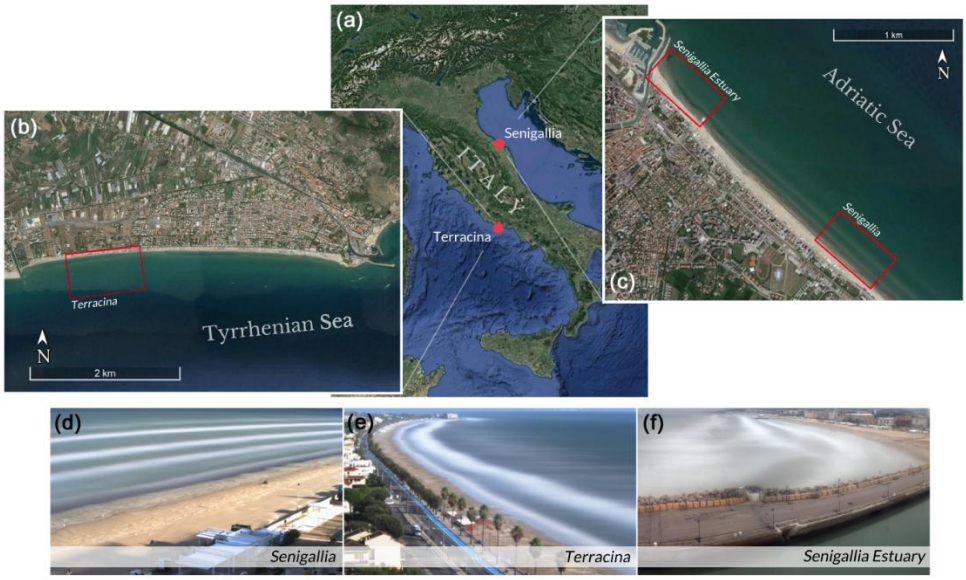

Figure 9. a) Map of Italy and locations of Senigallia and Terracina. b) Location of the video-monitored beach of Terracina. c) Locations of the video-monitored beaches of Senigallia Estuary and Senigallia. The bottom panels show examples of timex pictures used for the identification of bar crest locations at d) Senigallia, e) Terracina, and f) Senigallia Estuary.

Multi-annual sets of video imagery data from coastal monitoring stations have been analyzed to infer the position of sand bar crests as well as their displacement in response to wave attack. Beach images have been averaged to obtain timex images, in which the position of bar crests appear as white regions due to preferential wave breaking locations (Figure 9d-f). A semi-automatic algorithm is then applied to timex images to identify daily average shoreline and bar positions. To make up for the lack of wave buoys for in-situ measurements of wave climate, a 13-year wave climate hindcast to be compared with sand bar features has been extracted from the Mediterranean Sea Waves oceanographic model by the European Union Copernicus Marine Service (CMEMS).

The study has shown that the beach of Senigallia usually presents an array of three to four shore-parallel bars which are sensible to seasonal variations in wave climate (Figure 10). Bars exhibit overall seaward displacements of 0.09 to 0.26 m/day during generally more intense winter wave climate. Substantial bar inactivity was instead observed in summer months, when wave climate is milder. No significant response to single storm events was observed across the two-year analysis period. This global behavior is in stark contrast with the one observed at Terracina, where bar displacements appear to be more responsive to single storm events. This difference in response has been partly attributed to the different surf zone beach slope across the two sites.

Finally, sand bars in the stretch of beach closer to the Senigallia estuary jetty (Senigallia Estuary) has been found to be more susceptible to fairly large seasonal oscillations with respect to the behavior of the nearby unbounded beach of Senigallia, even though no discernible offshore or onshore migration trend was observed. This behavior was likened to an oscillation of the bar array around an equilibrium position, similar to that observed in both seasonal and interannual scales at the beach of Séte, France.

This study has highlighted how the response of underwater sand bars subjected to the same wave climate may be radically different whether or not they are influenced by the presence of engineering structures like those usually provided for the delimitation of river mouths.

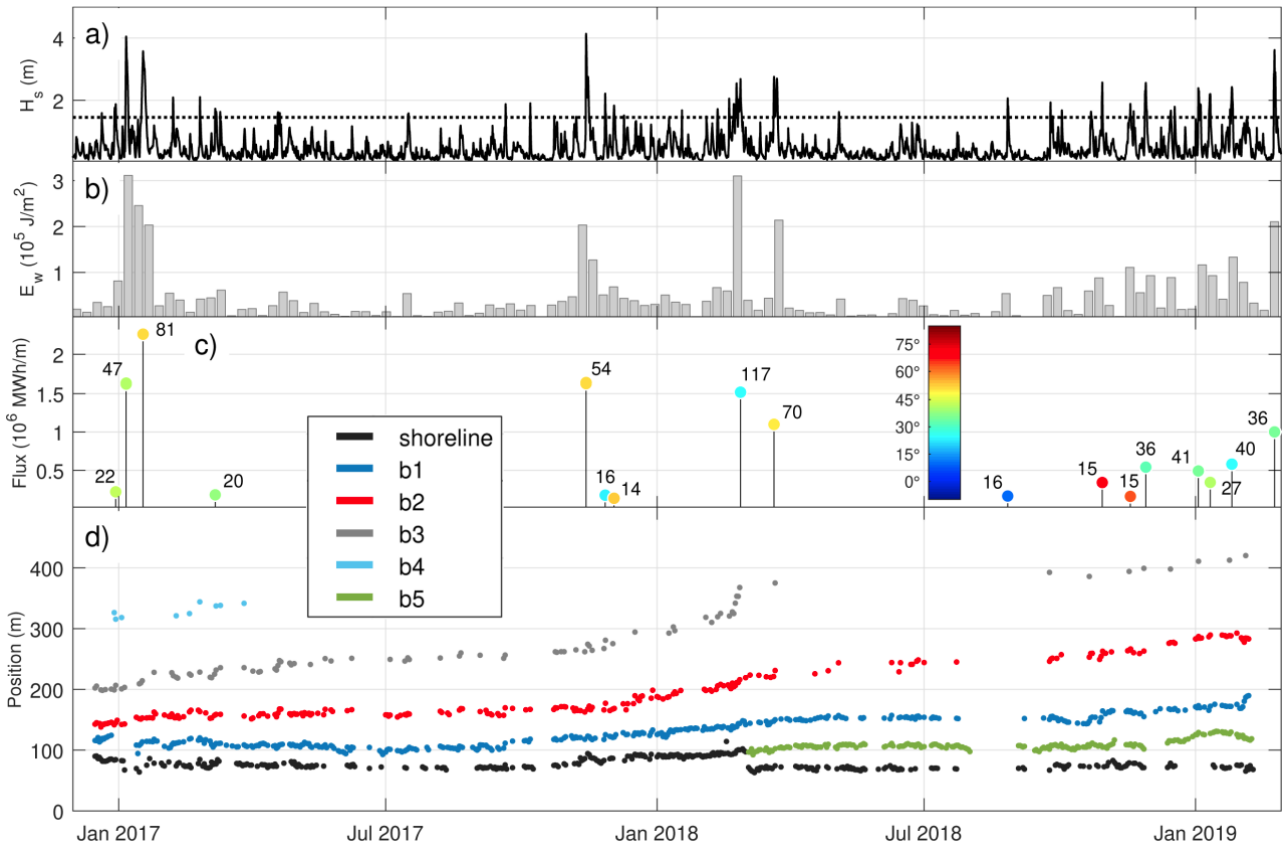

Figure 10. Wave climate and bar configuration in Senigallia (December 2016–January 2019). a) Modelled offshore significant wave height (solid line) and storm threshold (dashed line). b) Cumulated weekly wave energy. c) Characterization of classified storms. Stems length represents the energy flux. Numbers represent storm duration (in hours). Marker colours indicate the peak storm wave direction (°N). d) Cross-shore, alongshore-averaged bar and shoreline position.

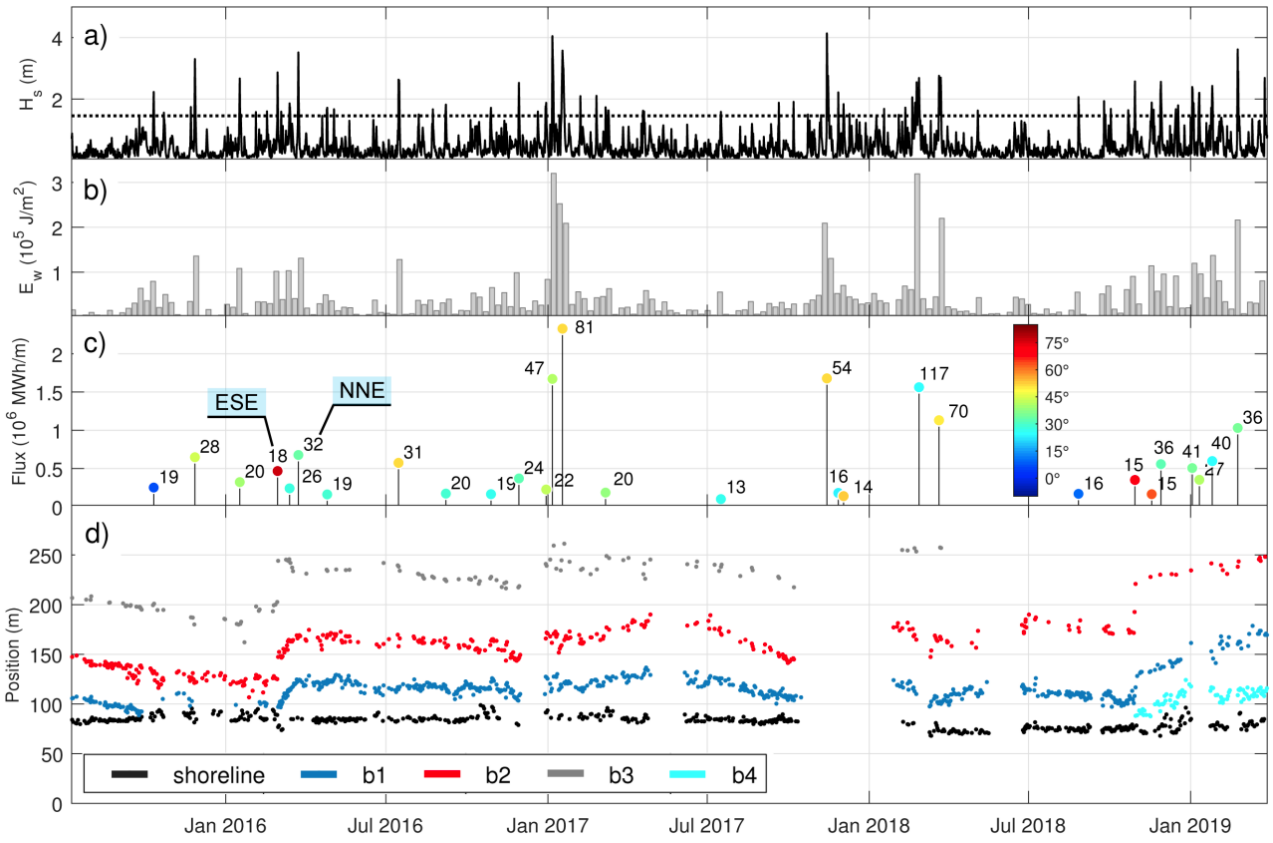

Figure 11. Wave climate and bar configuration in Senigallia Estuary (July 2015–March 2019). a) Modelled offshore significant wave height (solid line) and storm threshold (dashed line). b) Cumulated weekly wave energy. c) Characterization of classified storms. Stems length represents the energy flux. Numbers represent storm duration (in hours). Marker colours indicate the peak storm wave direction (°N). d) Cross-shore, alongshore-averaged bar position.

5.2.2 Mouth bar evolution

The MR is characterized by the presence of a mouth bar like many other Adriatic rivers. As described by Brocchini et al. (2017), such bar usually shows a cyclic behavior, with sediment accumulation during low flow periods (summer) and expulsion to sea during high flow periods (winter). However, the reduced precipitation of the last years led to the disruption of the sediment natural cycle and subsequent emergence of an unusually large inner mouth bar (Baldoni, 2021). Such sediment deposit at times filled the entire river section, causing concern among the population regarding the possible obstruction to the river flow during extreme events.

The work of Baldoni et al. (2021) demonstrated that even a moderate river discharge (comparable with the 1-year return period discharge) erodes the crest of the bar and causes sediment downriver migration. On the other hand, waves are responsible for sediment accumulation at the river mouth and slow upriver bar migration. Moreover, the upstream displacements due to 10-year return period waves are much smaller than downstream migrations due to moderate river discharges, confirming the dominance of the river action (Baldoni, 2023).

The study integrated both observations from the SGS video-monitoring station and Delft3D numerical simulations. A semi-automatic Matlab code was built to detect the bar from the images and extract timeseries of bar area and center of mass. Such information was then correlated with estuarine forces to identify the main mechanisms responsible for the bar evolution. Finally, after a preliminary model calibration, numerical simulations were run to better evaluate the effect of each force. Two river discharge peaks of 50m^3/s (R50) and 100m^3/s (R100), the latter comparable to the 1-year return period discharge, were tested with the wave

process turned off. On the contrary, to observe the effects of the waves only, two significant wave height peaks were tested: 2m (W2), a typical value for a storm interesting the Senigallia coast, and 5m (W5), comparable to the 10-years return period wave height, computed from the observations of the National Wave Buoy Network[3]. The wave direction was chosen on the basis of the most frequent storms occurring at Senigallia, thus NNE (N, 20°N) and E (E, 90°N). Some simulations were run with and without adding the tidal forcing, to observe its effect on the bar dynamics.

Results of the simulations are shown in Figure 12, where the evolution of an along-river section is reported. River discharges cause erosion of the bar crests and sediment deposition downstream, proportional to the discharge intensity (top panel). This was also confirmed by the analysis of the SGS images, showing that the bar always moved toward the river mouth after the occurrence of a river discharge peak (left panel of Figure 13). Numerical results showed that waves push sediments upriver, causing the crest of the most seaward bar to grow and move upriver (middle and bottom panels). As for the river discharge, also the displacement due to the wave action increases with the forcing strength. North-easterly waves, entering the estuary more easily, reach farther locations along the channel and modify the upriver portion of the deposit more than easterly waves. Slow upstream migrations during low flow conditions were also observed from the video-monitoring products (right panel of Figure 13). The tide has a marginal influence on the bar evolution.

The above analysis reveals that the MR inner mouth bar has a dynamical evolution, mostly affected by the river discharge and the waves, while the tide only modulates the action of the two main forces.

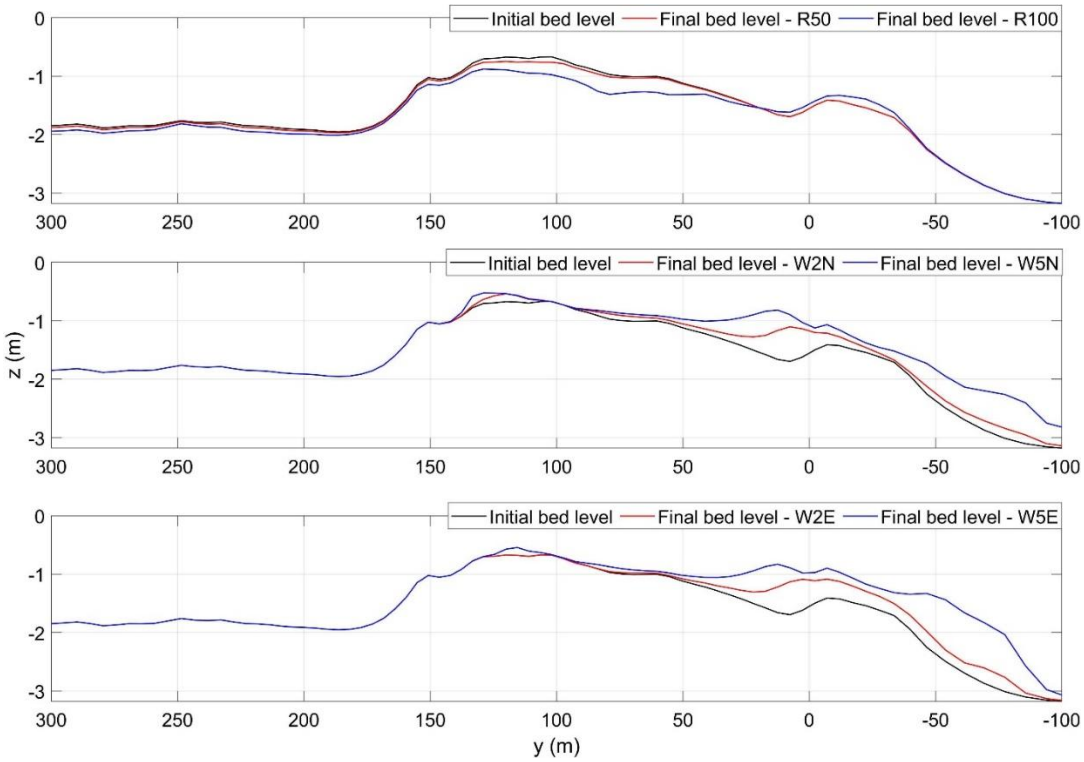

Figure 12. Modelled evolution of an along-river section (black line) subjected to river discharge (top panel), NNE waves (middle panel) and E waves (bottom panel). The origin of the y-axis is located at the river mouth; positive and negative y-coordinates represent, respectively, upriver and offshore locations. In the top panel, red and blue lines represent the final bed level for the simulations with Q=50m3/s and Q=100m3/s, respectively. In the middle and bottom panels, red and blue lines represent the final bed level for the simulations with maximum Hs=2m and 5m, respectively.

[3] HOMEPAGE (mareografico.it)

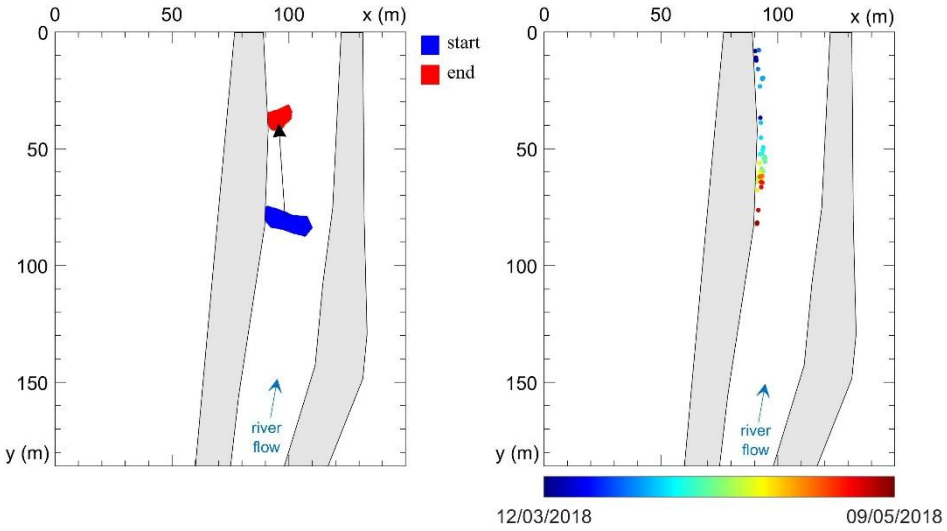

Figure 13. Results of image analysis. The left panel shows the bar before (blue) and after (red) the occurrence of a river discharge peak of about 35 m^3/s, highlighting the downriver migration. The right panel shows the center of mass of the bar from March to May 2018, colored depending on the day it was detected: the bar migrated upriver due to the wave action, since no river discharge events occurred during such period.

5.2.3 River plume

Despite its moderate size, the MR is characterized by large, suspended sediment transport that produces wide plumes. Factors influencing small-scale plumes are different from those typically affecting large to medium-scale systems, and less studied in the literature. The mechanisms responsible for the generation and spreading of the MR plume were studied integrating observations and modelling (Baldoni et al., 2022). Regarding the plume generation, the study focused on factors able to resuspend sediments at the river mouth. Therefore, in addition to the river discharge that is obviously the main generation mechanism, also the role of waves was investigated. In fact, from the analysis of optical images, the presence of suspended sediment was detected even in absence of discharge events, suggesting the existence of a secondary generation mechanism. Images from two shore-based stations were used: those from the SGS station (Figure 14, left) were used to track the plume front and determine its extension, while those from a station managed by ISPRA were used to qualitatively observe the plume spreading toward the south of the MR. Moreover, satellite images were also exploited to observe a wider area. The information retrieved from the image analysis was correlated with the estuarine forcing to recognize the plume generation and transport mechanisms. In a natural environment, the action of a specific forcing is difficult to isolate, since typically the observed physical phenomena are the outcome of a combination of several mechanisms. Therefore, Delft3D numerical simulations were run to separately study the effect of each force on the plume evolution. As done in Baldoni et al. (2021), simulations were run with 1) river discharge only (R50 and R100), 2) waves only (W2N, W2E, W5N, W5E) and 3) river discharge combined with different wind directions. Particle Tracking Velocimetry (PTV) was also performed on videos acquired by the SGS station (Figure 14, right) to obtain the surface velocity field in the final river stretch. However, the action of the river is not the only force to affect the plume evolution. At a river mouth, the interplay of multiple factors determines the velocity of the flow and the consequent extension of the plume.

Therefore, a further analysis was performed to compute the plume surface velocity, accounting not only for the action of the river, but also for wave and wind contributions.

Figure 14. Left: SGS time-exposure image showing a plume caused by the combination of river discharge and NNE waves. Right: video frame acquired by one of the SGS cameras, showing debris on the water surface that were detected by the PTV algorithm.

Delft3D results, in terms of plume extension, are shown in Figure 15. In the simulations, a background value for the suspended sediment concentration was imposed (0.05 kg/m^3), so that the plume area was identified as the area where the concentration exceeded the reference value. The river discharge alone produces plumes symmetrically distributed around the estuary, with extension proportional to the entity of the forcing (Figure 15, left). Simulations confirmed that waves are also capable of resuspending some sediment at the river mouth, producing plumes with an extension toward the offshore smaller than that produced by river discharges. As already observed for the bedload sediment transport (Baldoni et al., 2021), a river discharge comparable to the 1-year return period discharge generated a more extended plume with respect to 10-year return period waves. An analogous result was found for the suspended sediment concentration (see Baldoni, 2023). The mid and right panels of Figure 15 show that waves are also responsible for the alongshore spreading of the plume, pushing it further and further toward the coast as the forcing increases. Furthermore, simulations run with different wind directions, show that the wind determines the plume direction, with the plume offshore extension reducing at the increasing of the wind alongshore component. Numerical results agreed with observations and PTV findings. PTV analyses showed that the main contribution to the along-river plume velocity is due to the river discharge, while in the alongshore direction, the wind contribution is an order of magnitude larger than the wave contribution. The extension of the plume was correlated with the ratio between the along-river and alongshore components of the plume velocity, resulting in a one fourth pawer law. Thus, the plume extension increases with the along-river component of the velocity, largely determined by the river action. On the other hand, the plume offshore extension decreases for increasing alongshore component of the velocity, caused by wave- and wind-driven currents.

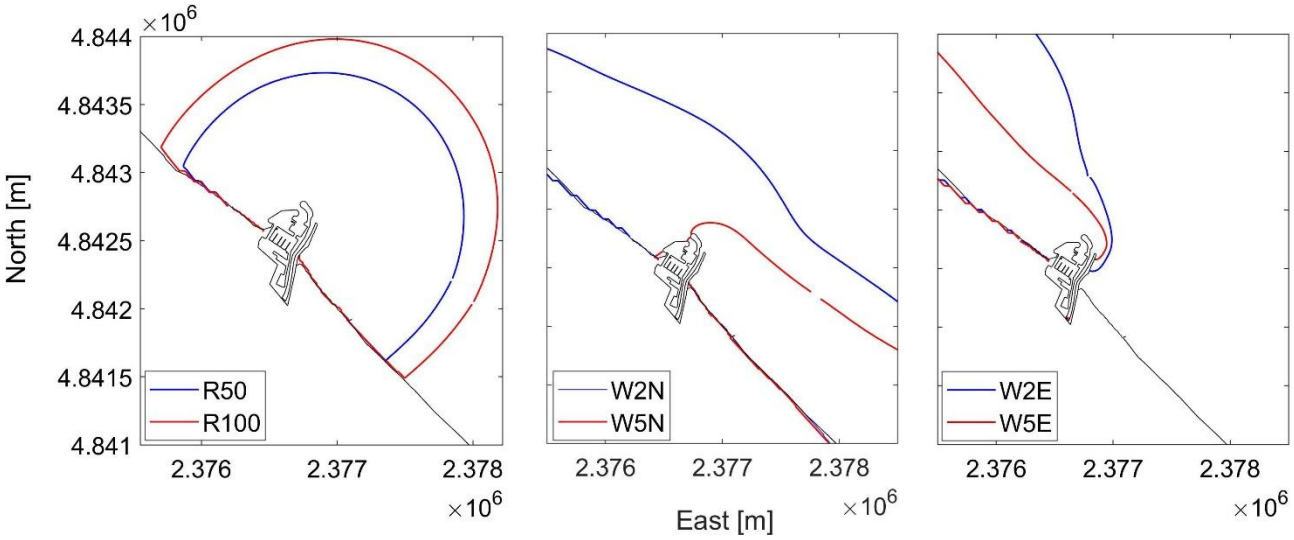

Figure 15. Modelled plume fronts generated by river discharges (left), NNE waves (middle) and E waves (right). In the left panel, blue and red lines refer to simulations with Q=50m^3/s and Q=100m^3/s, respectively. In the middle and bottom panels, blue and red lines refer to simulations with maximum H_s=2m and 5m, respectively.

5.2.4 Turbidity maximum

Many macro- and mesotidal estuaries are characterized by Turbidity Maxima Zones (TMZs). These zones are defined as regions with considerable higher suspended solid concentrations above typical background levels, primary due to enhanced sediment re-suspension related to shear along the estuarine bed (and, to a lesser extent, salinity induced flocculation) near the landward limits of salt intrusion or within the freshwater zone. The position and extent of TMZs is modulated and driven by tidal oscillations, especially in estuaries where tidal forcing is large. Although TMZs are typically associated with tidal forcing in meso-, macro- and hyper-tidal range estuaries, less prominent and ephemeral, storm-induced TMZs also occur and have been documented in microtidal systems. Observations at the microtidal MRE were performed in 2014 to study the hydrodynamics, morphological bed evolution, and water physio-chemistry of the MR during quiescent periods, stormy and transitional period between storms (Postacchini et al., 2023). Data was collected during a big Bora storm, a smaller storm and the quiescent period between them. In addition, simulations of flocculation dynamics were run, using an existing model suite (e.g. Manning et al., 2011), for three scenarios, i.e. small storm, big storm and transition between the storm events.

Generally, 300 m upriver of the MR mouth, the sea action (wind, wave, tides) is larger than the freshwater forcing (river discharge), thus promoting an overall net landward flow of seawater in the lower portion of the water column during quiescent periods, whereas fresh water flows gravitationally seaward in the upper portion of the water column. The higher tide level, the thicker the seawater-intrusion layer.

Results show that, during moderate-flow regime (represented by the smaller storm), waves propagated inside the MR, facilitated by low river flow. The hydrodynamic conditions in the lower reach of the MR changed, transitioning from a salt-wedge behavior during quiescent conditions to a mainly cross-river flow. During this regime, a strong interaction between river and sea took place, and significant sediment re-suspension occurred as a consequence both of the river- and wave-driven fast flows and of the high shear stress. An ephemeral

TMZ developed whit high turbidity near the bed at the leading edge of the seawater tongue (see the separation between green and blue shades in Figure 16a). The estuary was well-stratified in its upriver/landward portion. Furthermore, significant flocculation and fast macrofloc settling occurred where the TMZ generates.

On the other hand, during high-flow regime (represented by the big storm), the wave height abruptly decreased at the MR mouth due to breaking and being opposed by a significant freshwater outflow. In such conditions, the river prevailed, resulting in a homogeneous freshwater column characterized by seaward flow across the entire water column and expulsion of sediments to sea. Compared to what observed during the small storm, the upriver region of the estuary was characterized by smaller turbidity gradients and a weaker stratification (Figure 16b). Results suggest an increase of turbulence and mixing during the BS, which led to a reduced flocculation, a slower settling and a greater particle dispersion within the water column which, in turn, promoted TMZ suppression near the riverbed.

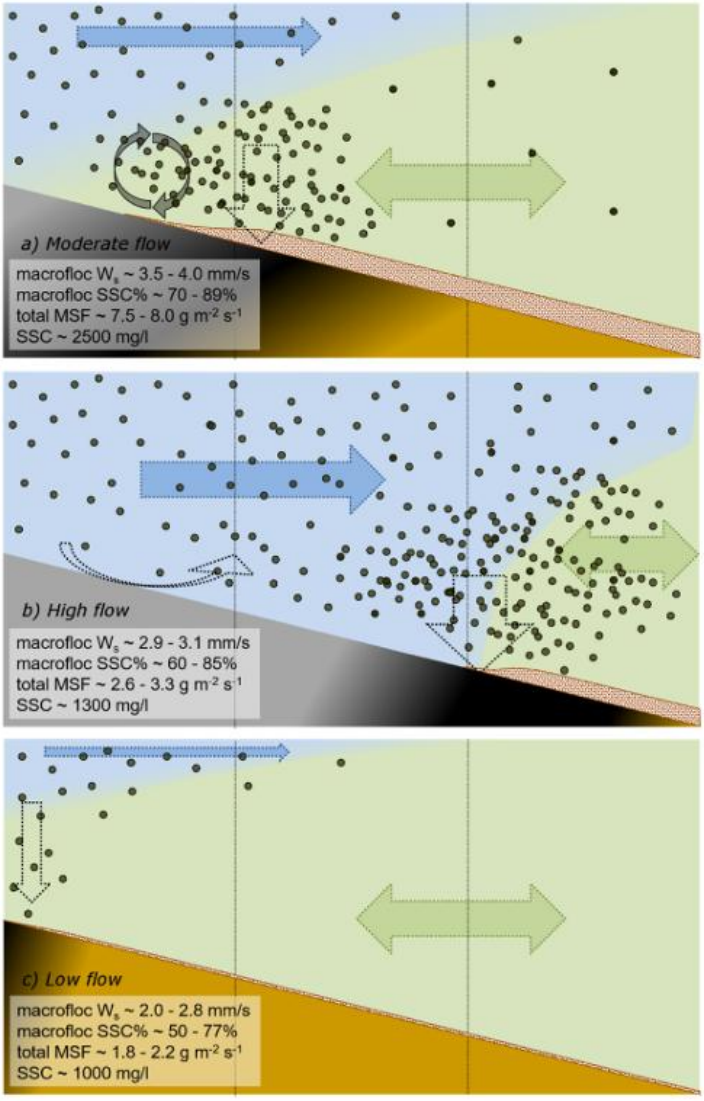

Figure 16. Conceptual model representing: a) moderate-flow conditions (SS); b) high-flow conditions (BS); c) low-flow conditions (transition). Blue shades and arrows identify the river forcing. Green shades and arrows identify sea forcing (waves and tides). Black and grey arrows show the sediment-particle motion. The vertical thin lines qualitatively indicate instrument locations.

Low-flow conditions lead to relatively high turbidity values associated with the freshwater tongue of the MR in the upper water column and sea intrusion in the lower part, with upriver-downriver flow separation continually modulated by the tide (Figure 16c). A combination of salinity-induced flocculation and bio-cohesion potentially occurs in the final reach, causing settling of fines close to the mouth and increasing their residence times within the estuary.

5.2.5 Modeling chain

To model the wave propagation from offshore towards the coast, including the interaction with obstacles, such as harbors or defense structures, a modeling chain has been implemented. A combination of two numerical models is used. The former is a *wave-averaged* model, Delft3D, that gives a wave description averaged over the wave period. To simulate the evolution of waves, Delft3D WAVE (Delft3D-WAVE User Manual) uses the third-generation SWAN model (Booij et al., 1999), developed at Delft University of Technology (The Netherlands). The SWAN model is based on the discrete spectral action balance equation and allows one to simulate the wave propagation over large domains in a relatively short time. However, it has limitations when dealing with large seabed gradients, as for example near harbors or barriers for coastal defense. Therefore, a *wave-resolving* model, either XBeach or FUNWAVE, which computes velocities and water levels for all wave phases in the wave period, is also used. XBeach (XBeach-homepage) is an open-source two-dimensional model for propagation of short waves (refraction, shoaling, breaking) and long waves (infragravity waves), wave-induced set-up and run-up, overwash and inundation. XBeach is used in a wave-resolving (non-hydrostatic) fashion, thus requiring higher computational power. FUNWAVE (Shi et al., 2012) solves the non-linear Boussinesq equations for modeling surface wave transformation from deep water to the swash zone, as well as wave-induced circulation inside the surf zone. Model applicability in shallow waters has been implemented and extended in recent years thanks to the possibility of representing physical processes, such as wave breaking and swash zone dynamics, through the automatic transition from a Boussinesq-type model to a shallow water model whenever the Froude number exceeds a certain threshold.

Delft3D is used to transfer the wave from water depths of almost 20m, at which the boundary conditions are prescribed, to water depths of around 8m. The resulting wave characteristics are then used to force the wave-resolving model that computes the propagation of the wave towards the shoreline. Such a model is also capable of computing the inundation perimeters. A similar methodology, based on a modeling chain, was used to describe the coastal inundation in different contexts: from flooding caused by present meteo-marine forcing on relatively steep coasts (Postacchini et al., 2019), to inundation triggered by future scenarios on mildly sloping beaches (UNIVPM study for the Marche Region within the CASCADE Project, 2023).

To simulate compound flooding, generated by the combination of river and sea actions, a new detailed model is under evaluation. In fact, if a river discharge must be included in the simulation, FUNWAVE cannot be used. Moreover, when including a combination of forcing and the morphology computation in quite large domains with high grid resolution, the computational time required by XBeach becomes too large. Therefore, a Delft3D-FM (D-Flow_FM_User_Manual) detailed model is under development. It extends 1.6km and 1.4km, respectively offshore and landward of the MRE. Flexible meshes allow one to 1) adapt the grid to the geometry of the site and 2) refine the grid locally, increasing the resolution only in areas of interest, this reducing the computational effort.

5.3 Gulf of Cagliari

In the Gulf of Cagliari, a low-cost computational warning system capable of predicting storm flooding on the Poetto beach four days in advance has been tested. This operational wave system, replicable in similar contexts, can serve as a key tool for decision makers and stakeholders in various coastal and maritime sectors. The system currently operates in two test areas surveyed by two video-monitoring systems that validate the model.

Wave motion simulations are carried out on series of grids grafted for wave transport from offshore to shore, at increasing levels of detail. On the sample beach, in order to have a wave data representative of near-shore conditions, the wave outside the breaker zone is obtained by propagating the sea state with a spectral wave model.

The offshore incident wave prediction, obtained from the Copernicus Marine Service CMEMS database, is propagated in the coastal waters with the SWAN wave model to the outer boundary of the storm surge zone. To complement the wave data, the hydrodynamic parameters of mean sea level, resulting from the sum of storm surge and astronomical tide, are extracted from the CMEMS system.

In addition to the conditions on the open contour, the model is forced by the wind obtained from the ECMWF series. The EMODnet (European Marine Observation and Data Network) bathymetry was identified as the bathymetric basis for the resolution of the main wave transformation processes in coastal waters, which is supplemented by constantly acquired and updated detailed bathymetry.

CMEMS data is processed prior to the simulation in order to reconstruct the direction and frequency spectra from the spectral parameters provided by CMEMS. The spatial domain is about 10-15 km, which would always be best to be complemented by a coastal video monitoring system. The spatial resolution is approximately 100 m and the simulation is performed in stationary mode for each identified swell. In this way, coastal refraction processes are reproduced and, for each swell, representative wave parameters are obtained at the breaker zone.

Initial and boundary conditions for the morphodynamic simulations are represented by three-dimensional models of the seabed and sediment distribution areas reconstructed from data derived from bathymetric and sedimentological surveys. In addition, wind forcing is considered using forecast data provided by the European meteorological centre ECMWF.

The SWAN model output data in the breakwater zone, combined with topographic and bathymetric data from the surveys, are then used as input to the parametric runup formulation, following Stockdon's formula. Finally, the tidal and storm surge elevation is added to the runup elevation derived from the parametric formulation, thus obtaining the total water level, which, based on the berm elevation measured during the periodic surveys, tells us whether or not flooding will occur.

This model will later be implemented, replacing the parametric component with a detailed model, such as XBeach, for an even more accurate prediction that also takes into account the infiltration parameters, the topography and the presence or absence of banquette and other wooden debris on the emerged beach.

5.4 Cuba-Longarini coastal wetlands

The "Pantani della Sicilia Sud-Orientale" (Lagoons of the South-East of Sicily) is a Mediterranean coastal wetland ecosystem in the Southeastern tip of Sicily, Italy (Figure 17a), characterized by a significant interaction between the hydrographic network, the dune, the beach and the sea as well as by significant anthropic and climatic pressures.

This region spans roughly 35 km^2 across a 90-km stretch of coastline, featuring a network of eight primary lagoons interspersed within the surrounding dunes and beach environments. The beaches, predominantly narrow and sandy, are punctuated by rocky promontories and islands. These lagoons receive water primarily through small catchments (O(1-10) km^2), particularly during the intense flash floods seen from October to December. Seasonally, the water levels within these lagoons exhibit significant fluctuations, oscillating between 1 to 2 meters in the winter to complete dry conditions during the summer months, with salinity fluctuations from 5 to 30 PSU.

Among these wetlands, the Cuba-Longarini complex is the largest, covering about 3.50 km^2 (Figure 17). The Cuba lagoon to the East spans roughly 0.80 km^2, while the Longarini lagoon to the West covers about 1.80 km^2. Located along the central migratory flyway of the Mediterranean, this area witnesses the annual migration of birds, making it a crucial winter haven for numerous waterfowl species and a breeding ground for fish and crustaceans.

Thanks to its unique climatic conditions and rich biodiversity, the site has gained international recognition, being designated as part of the Natura 2000 network, which includes both Special Areas of Conservation (SACs ITA090003) and Special Protection Areas (SPAs ITA090029) under the European Union's Habitats and Birds Directives. Several species within this area are categorised as vulnerable or endangered, as listed on the IUCN Red List of Species.

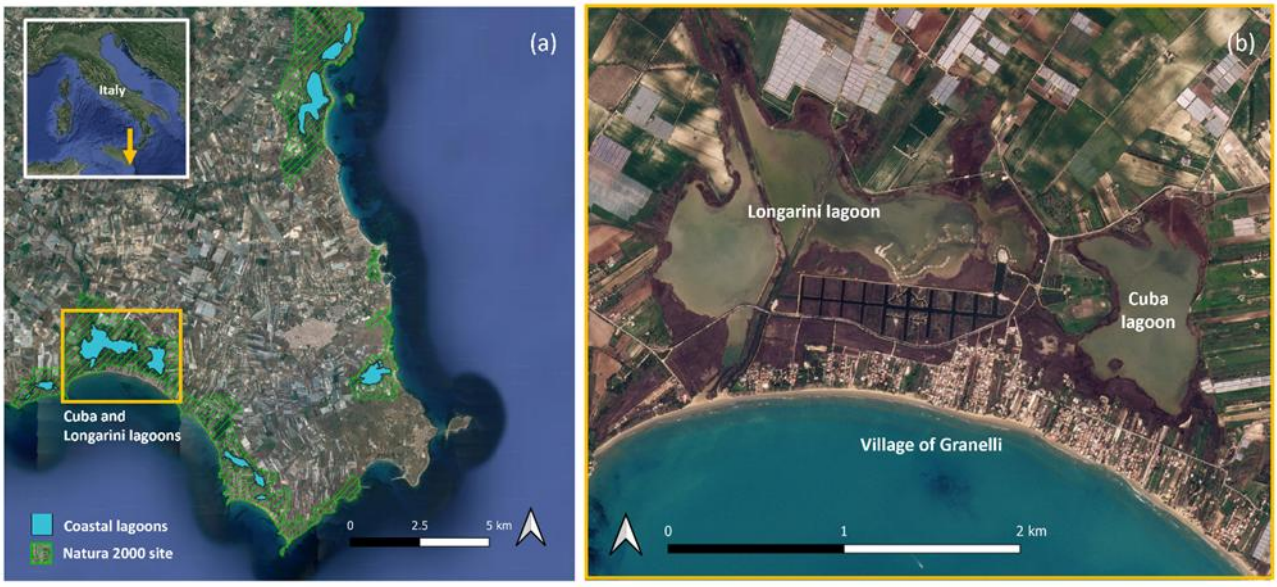

Figure 17. a) aerial view of the “South-East of Sicily lagoons” region, b) aerial view of the coastal lagoon complex Cuba-Longarini and the beach village of Granelli

However, this region is under threat due to human activity. Over the past fifty years, there has been a noticeable shift from traditional farming to intensive agricultural practices, adversely affecting the water quality and the area's overall hydraulic and hydrological stability. Concurrently, its popularity as a tourist destination has led to chaotic urban expansion at the expense of wetlands and dunes. An archetypical example is the village of Granelli, located between these lagoons and the sea, which disrupts the natural dune barrier, diminishing the area's resistance to flooding and erosion (Musumeci et al, 2022; Marino et al., 2023). This disruption is compounded by the threats of climate change, with increasing occurrences of river floods, marine storms, and Medicanes, and hazard related to sea-level rise expected by the end of the century, posing a significant risk to the region's sustainability and ecological integrity (Antonioli et al., 2020; Musumeci et al, 2022).

5.3.1 Data description

Present wave conditions were obtained from the MEDSEA MULTIYEAR WAV 006 012 reanalysis dataset (Korres et al., 2021) provided by the Copernicus Marine Service, spanning 1993-2022 with hourly time series and a spatial resolution of 4.66 × 4.66 km. Climate change projected wave conditions were taken from "Ocean surface wave time series for the European coast from 1976 to 2100 derived from climate projections dataset" (Caires et al., 2020). This dataset provides hourly time series of marine wave climate from 2041-2100 with a spatial resolution of 30 x 30 km. Wave conditions were projected for two IPCC AR5 scenarios, RCP4.5 and RCP8.5. Significant wave height (H_s), peak period (T_p), and mean wave direction (θ) were extracted for present, RCP4.5, and RCP8.5 scenarios, closest to the offshore boundary (latitude 36.69°N, longitude 15.00°E).

Sea level rise projections based on IPCC AR6 are considered (Fox-Kemper et al., 2021). In IPCC AR6, RCPs are combined with Shared Socioeconomic Pathways (SSP) (Riahi et al., 2017). Specifically, AR6 investigates five SSP-RCP joint scenarios. For consistency with offshore wave climate projections based on IPCC AR5 RCP4.5 and 8.5, IPCC AR6 sea level projection scenarios SSP2-4.5 and SSP5-8.5 were used. Data were extracted using the NASA Sea Level Projections tool, for geographical coordinates closest to the site (latitude 36.00° and longitude 14.00°), for the years 2070 and 2100.

A numerical modelling chain is used made up by a larger SWAN model, which allows wave propagation to the coast, and a detailed XBeach model, able to describe coastal processes in the presence of compound flooding and taking into account the influence of vegetation (and of Nature-based solutions). To build the SWAN numerical grid, bathymetric contours were taken from nautical charts (Istituto Idrografico della Marina, 2019). For the XBeach numerical grid, a Digital Elevation Model (DEM) from the Regional Geographic Information System of Sicily Region, obtained through LiDAR flights in 2013, was used. The DEM was combined with bathymetric data from a multi-beam survey carried out by the University of Catania in 2019, integrated with satellite images, drone data, and field surveys, including small artificial islands and channels built in 2023. The shoreline was obtained through PlanetScope satellite imagery by tracking the wet/dry boundary. Elevations from DEM, bathymetry, and shoreline were combined to assign elevation at the XBeach grid nodes through linear interpolation. Sediment sample surveys at Granelli beach showed well-sorted fine sand with D_{50} = 0.26 mm and D_{90} = 0.29 mm.

The XBeach model simulates wave dissipation due to vegetation. Spatial distribution and physical characteristics of the vegetation were given as input parameters. Distribution data were obtained from Carta della Natura and confirmed by field surveys. Physical characteristics such as vegetation height, vertical sections, number of stems per m², stem diameter, and drag coefficient were sourced from relevant literature

(Knutson & Smith, 1982; Garzón et al., 2019; Fernández et al., 2020; Musumeci et al., 2022) and revised by local experts.

5.3.2 Model setup

A modelling chain is set up to simulate the hydro-morphodynamics resulting from extreme wave events within the case study (Figure 18). The model integrates a hydrodynamic model, which solves wave propagation from offshore to nearshore (SWAN, Booij et al., 1996), and a morphodynamic model for predicting flooded areas and shoreline change (XBeach, Roelvink et al., 2009).

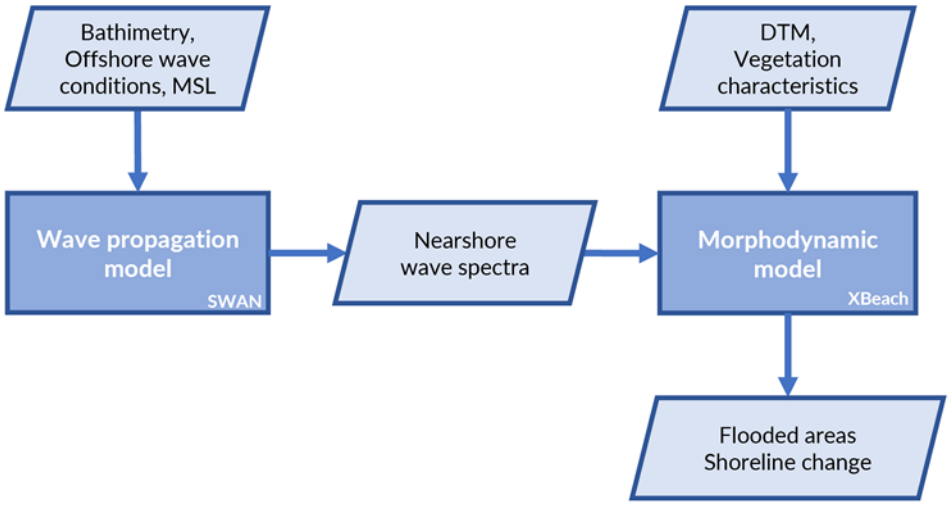

Figure 18. The modelling chain flowchart

The SWAN computational domain covers 2068 km^2 and approximately 90 km of coastline (Figure 3a), with a grid of 17141 nodes. Grid resolution varies based on bathymetry, ranging from 1 km for depths over 100 meters to 400 meters for depths under 30 meters, with a higher resolution of 100 meters near the XBeach domain.

The XBeach domain (

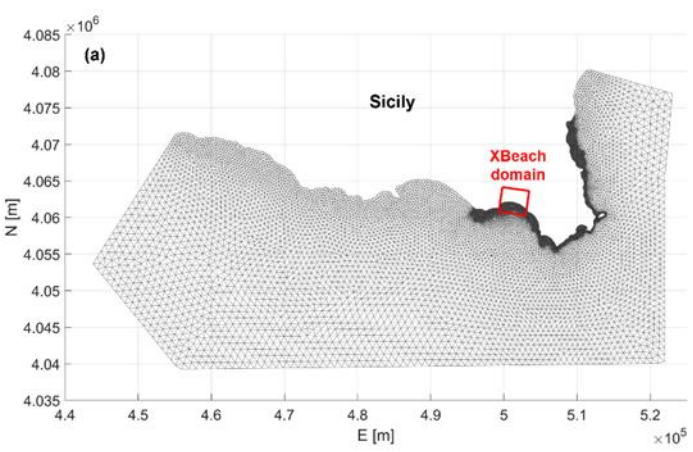

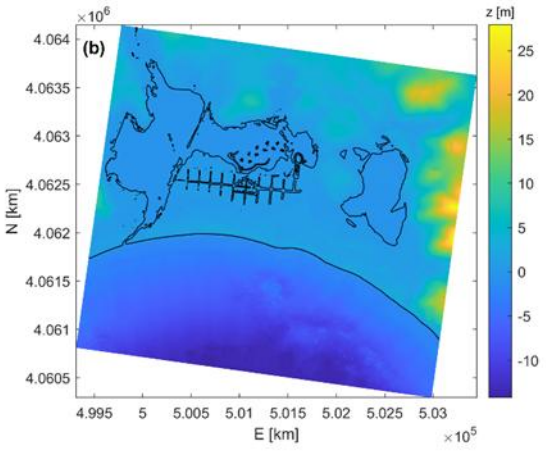

Figure 19) is nested within SWAN, spanning 3.36 km cross-shore and 3.69 km long-shore, totaling 12398 km^2, including the Cuba-Longarini lagoon system, Granelli town, and beach. The structured grid varies from 2.5 to 10 meters cross-shore and 5 to 10 meters longshore, with 1150 cross-shore by 544 long-shore cells, totaling 625,600 nodes.

Elevation values for each cell node are derived from a Digital Elevation Model (DEM) combined with coastline data obtained from satellite imagery. Elevation ranges from -14.22 meters to 27.92 meters, with missing areas (approximately 0.27 km^2) interpolated. Panel b depicts elevation values within the XBeach domain.

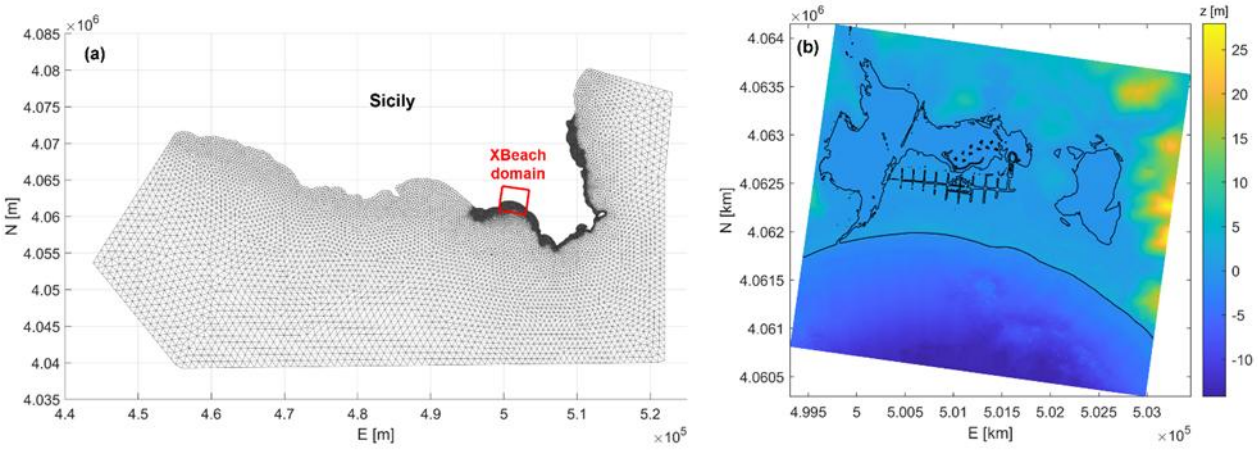

Figure 19. SWAN model domain and grid, (b) XBeach elevation z within the domain, with z = 0 m denoted by the black line.

The XBeach model simulates wave dissipation due to the presence of vegetation by implementing a dissipative term in the short-wave action balance equation. For each habitat within the study area, a representative vegetation species is assigned based on a cross-comparison between habitat maps and field surveys. Four species were selected as representatives of four habitats. Vegetation distribution maps used as input for XBeach are shown below:

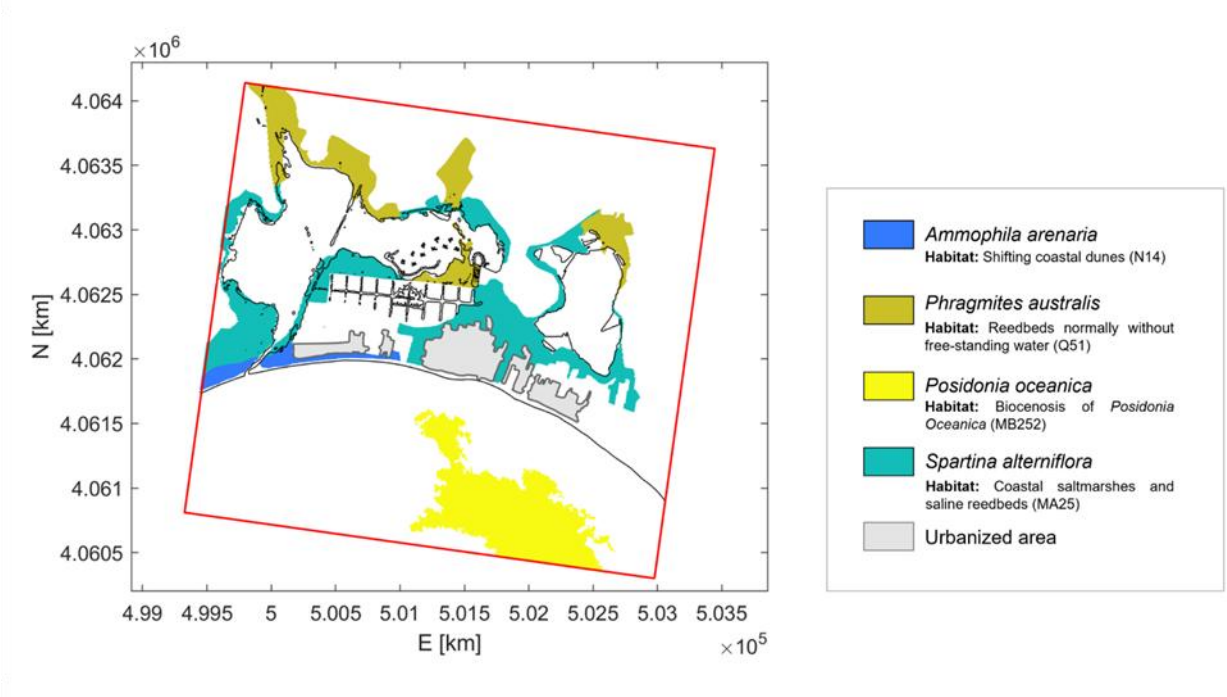

Figure 20. Vegetation distribution map used as input for the XBeach model

5.3.3 Definition of hydrodynamic scenarios

The categorisation of events based on their significant wave height Hs and wave direction was also carried out to identify the prevailing direction and the direction associated with the most energetic sea states. The entire wave direction sector, spanning 120° from 150° North to 270° North, was divided into eight sub-sectors of 15° each. An extreme value analysis was conducted for each sub-sector to find the Hs associated with storms with a 100-year return period (Tr). This analysis used a consistent 30-year window for both present (1993-2022) and future scenarios (RCP4.5 and 8.5) achieved through two separate 30-year windows (2041-2070 and 2071-2100) for the future.

The analysis involved the following steps. The Peak-Over-Threshold method identified wave peaks exceeding a 2.0-meter threshold within the Hs time series. A minimum time gap of 12 hours separated independent storm events (Boccotti, 2004). Different probability distributions (Weibull, Gumbel, LogNormal, and Generalized Pareto) were compared to the storm Hs data to find the best fit using the Kolmogorov-Smirnov test. The Generalized Pareto distribution provided the best fit for extreme Hs values within each sub-sector. A 100-year return period Hs value, commonly used for designing coastal protection structures, was extracted from the fitted Generalized Pareto distribution for each sub-sector.

The analysis revealed a dominance of extreme events originating from the west direction (255° - 270° North). Consequently, further analysis focused on this specific sub-sector.

Site-specific relationships between Hs and peak wave period (Tp) were established for present and future scenarios (RCP4.5 and 8.5) using the least squares method. The resulting equations are:

$$T_p = 6.6301 H_s^{0.2593}$$

$$T_p = 6.3327 H_s^{0.2867}$$

$$T_p = 6.3224 H_s^{0.2892}$$

for present, RCP 4.5 and RCP 8.5 respectively.

Sea level rise projections based on IPCC AR6 are considered in the present work (Fox-Kemper et al., 2021). In IPCC AR6, to explore potential climate change impacts based on both levels of greenhouse gas emissions and socioeconomic conditions, RCP are combined with Shared Socioeconomic Pathways, or SSP (Riahi et al., 2017). SSP offer a set of scenarios (SSP1-5) that span from more optimistic to less optimistic outlooks for the future, providing different narratives for how society, demographics, economics, and technology might evolve over the 21st century. Specifically, the AR6 investigates 5 SSP-RCP joint scenarios, combining three SSP (SSP1, SSP2, and SSP5) with the RCP associated with the anticipated level of radiative forcing by the year 2100 (ranging from 1.9 to 8.5 W/m²).

To be consistent with the available offshore wave climate projections data, which are based on IPCC AR5 RCP4.5 and 8.5, IPCC AR6 sea level projection scenarios with the same radiative forcing are considered in the present work, namely SSP2-4.5 and SSP5-8.5. Data were extracted using the NASA Sea Level Projections tool (NASA, 2024) at the closest geographical coordinates to our site (latitude 36.00° and longitude 14.00°). The projection of mean sea level is extracted for the years 2070 and 2100, to be consistent with the time horizons of the extreme wave analysis.

Offshore wave climate and sea level rise scenarios were combined to obtain a range of hydrodynamic scenarios to be investigated. Specifically, we investigated 5 hydrodynamic scenarios: a present scenario (SP), two climate change projection scenarios associated with radiative forcings equal to 4.5 W/m² with 2070 and 2100 time horizons (S4.5-2070 and S4.5-2100 respectively), and two scenarios for radiative forcing equal to 8.5 W/m² (S8.5-2070 and S8.5-2100 respectively). The investigated hydrodynamic scenarios are listed in the table below.

Table 2. Investigated hydrodynamic scenarios. Wave characteristics are obtained by extreme value analysis for T_r = 100 years with a 30-year time window for present and RCP scenarios. Sea level rise data are obtained from SSP scenario sea level local IPCC AR6 projections.

Hydrodynamic scenario	Time window [years]	H_s [m]	T_p [s]	SLR [m]
SP	2041 - 2070	6.01	10.56	0.00
S4.5-2070	2071 - 2100	8.70	11.77	0.37
S4.5-2100	2041 - 2070	7.75	11.39	0.57
S8.5-2070	2071 - 2100	6.97	11.09	0.48
S8.5-2100	2041 - 2070	9.18	12.00	0.78

5.4 Venice Lagoon

The Venice Lagoon, Italy (Figure 21a) is the largest brackish tidal basin of the Mediterranean Sea, with an area of about 550 km^2. The Lagoon formed over the last 7500 years covering alluvial Late Pleistocene, silty-clayey deposits locally known as *Caranto* (Zecchin et al., 2008). The Lagoon's present-day morphology is characterized by the presence of three inlets, namely, from North to South: Lido, Malamocco, and Chioggia (Figure 21a-d). Tides follow a semidiurnal microtidal regime, with a mean spring tidal range of 1 m and maximum tidal oscillations of about 0.75 m around Mean Sea Level (MSL) (e.g., D'Alpaos et al. 2013; Valle-Levinson et al. 2021).

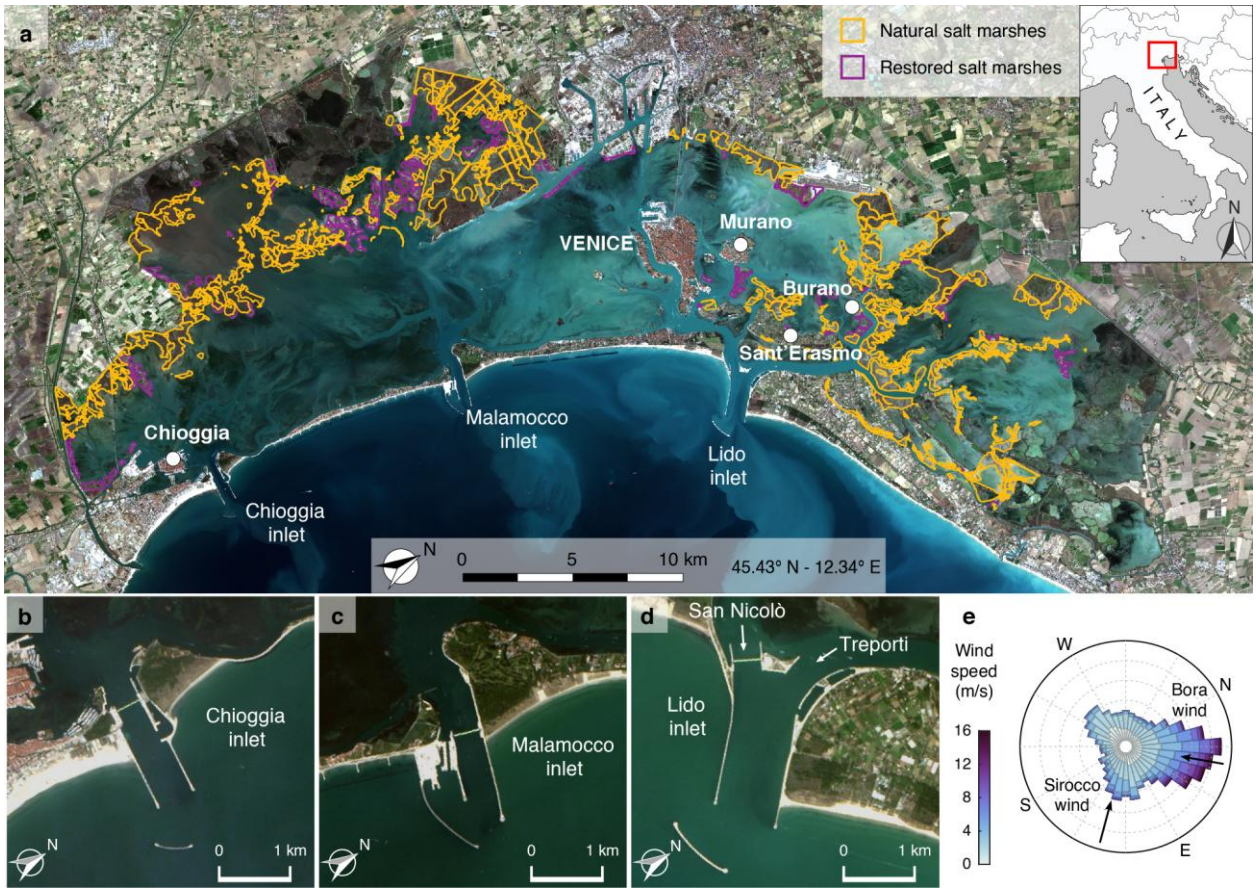

Figure 21. Geomorphological setting. (a) Satellite images of the Venice Lagoon (image Copernicus Sentinel, 2020). Natural salt marshes are bordered in yellow, while restored salt marshes are shown in purple. (b, c, d) Close-up views of the three lagoon inlets. (e) Rose-diagram representation of wind climate recorded at the "Chioggia Diga Sud" anemometric station during the period 2000-2019. The two most relevant winds, i.e., the north-easterly Bora wind and south-easterly Sirocco wind, are also highlighted.

Meteorological surges often overlap astronomical tides, thus producing significantly high (low) tides when atmospheric pressure is low (high). In addition, wind-related processes are critical for both the hydrodynamics and morphodynamics of the lagoon, with seasonal wind-storm events exerting a prominent morphodynamic control over decadal to centenary timescales (see Carniello et al. 2009, 2012). The most morphologically and hydrodynamically meaningful wind-storm events are those associated with *Bora* and *Sirocco* winds (Figure 21e). The north-easterly *Bora* winds blow almost parallel to the major axis of the lagoon, thus producing

pronounced water-level setups in the southern lagoon and generating large waves (significant wave height H_s>1 m). Such waves promote significant resuspension of sediments from the tidal mudflats. In contrast, *Sirocco* winds blow from the South-East and cause large water-level setups in the northern Adriatic Sea, often leading to extensive flooding of Venice city and other settlements within the lagoon.

Over the last centuries, the hydrodynamics of the lagoon was severely affected by anthropogenic interventions (L. D'Alpaos, 2010; Ferrarin et al., 2015). First, by the end of the 16th century, all the major rivers debouching into the lagoon were diverted into the open sea, thus almost completely eliminating fluvial sediment input. Second, between the 1900s and 1970s, extensive land reclamation projects were carried out, especially along the landward margin of the lagoon, thus importantly reducing the total area open to the propagation of tides. During the same period, the extraction of groundwater and natural gas for industrial purposes significantly accelerated the natural rates of soil subsidence (Carbognin et al., 2004; Gatto & Carbognin, 1981; Zanchettin et al., 2021). Moreover, in order to allow for increasingly bigger ships to cruise within the lagoon, two large waterways, namely the Vittorio Emanuele and the Malamocco-Marghera channels, were excavated in 1925 and 1968, respectively. Major changes in the lagoon hydrodynamics were due to the construction of jetties at the lagoon inlets aimed to ensure water depths suitable for commercial ship traffic (Figure 21b-d). The jetties at the Malamocco inlet were constructed between 1839 and 1872, whereas at the Lido inlet the northern jetty was completed in 1887, with the southern jetty added later in 1892. Finally, the jetties at the Chioggia inlet were built between 1910 and 1934. On the one hand, the jetties reduced the width of the inlets, thus resulting in considerable deepening as foreseen during the design phase. On the other hand, they caused critical changes in the lagoon hydro- and morpho-dynamic regimes. Since the construction of the jetties, changes in the tidal regime within the lagoon have been much more sustained than the typical periodic, multi-annual variations induced by the nodal modulation of tides in the Adriatic Sea, which are in the order of 4% of the characteristic tidal range (Amos et al., 2010; Valle-levinson et al., 2021). Between 1909 and 1973, the tidal range within the lagoon increased as much as 25% on average (L. D'Alpaos, 2010; Ferrarin et al., 2015; Tomasin, 1974), with local changes that can be even more pronounced (Finotello et al., 2019, 2022; Silvestri et al., 2018).

Changes in the lagoon hydrodynamics due to the construction of the jetties, coupled with eustatic sea-level rise (average value 1.23±0.13 mm/year between 1872 and 2019; 2.76±1.75 mm/year between 1993 and 2019; see Zanchettin et al. 2021), critically impacted on the lagoon morphological evolution, triggering positive morphodynamic feedbacks. Progressively larger portions of the lagoon became ebb-dominated, especially close to the inlets where the jetties produced strong flow asymmetries. Asymmetric tidal flows enhanced the export of fine sediments and prevented the import of sediment carried in suspension by longshore currents (L. D'Alpaos, 2010). This condition, worsened by anthropogenically-induced starvation of fluvial sediments, set a negative sediment budget and resulted in a generalized loss of salt marshes (Carniello et al., 2009; L. D'Alpaos, 2010; Tommasini et al., 2019). Reduced marsh coverage lengthened wind fetches, thus favoring the formation of higher, more energetic waves, which further enhanced lateral marsh retreat and prompted erosion of tidal mudflats (Carniello et al., 2009; Finotello et al., 2020; Leonardi, Ganju, et al., 2016; Marani, D'Alpaos, et al., 2011; Mariotti & Fagherazzi, 2013; Tommasini et al., 2019). Mudflat deepening, exacerbated by eustatic sea-level rise and both natural and anthropogenic-induced subsidence, promoted the formation of even higher wind waves, which in turn favored additional erosion of salt marshes and mudflats through a positive feedback loop.

Further manmade modifications of the inlet morphologies were carried out between 2006 and 2014 to accommodate the mobile floodgates of the Mo.S.E. (acronym for "Modulo Sperimentale Elettromeccanico", Electromechanical Experimental Module) system (Figure 21b,c,d), designed to protect the city of Venice and other lagoon settlements from extensive floodings (R. A. Mel et al., 2021). These interventions slightly

increased hydraulic resistances at the inlets and led to both a reduction of tidal amplitudes and an increase in tidal-phase delays within the lagoon (Ghezzo et al., 2010; Matticchio et al., 2017). Salt-marsh erosion is still ongoing nowadays, though at much lower rates compared to the last century. This is due to a series of critical interventions, aimed at safeguarding and restoring salt marshes, that have been put in place by the Venice Water Authority since the early 1990s, with additional more recent contributions by some EU-funded LIFE projects (Barausse et al., 2015; Tagliapietra et al., 2018; Tommasini et al., 2019; see also www.lifevimine.eu/ and www.lifelagoonrefresh.eu/). At present, about 12 % of the existing salt marshes are either entirely artificial or at least partially restored (see purple lines in Figure 21a), and a good portion of the remaining natural ones are protected against lateral erosion by manmade wood piling or berms. Clearly, without these restoration and conservation efforts, the total area of salt marshes would be significantly smaller than it currently is.

The loss of geomorphic diversity of the Venice Lagoon has been further exacerbated by the regulation of tidal flows through the Mo.S.E. floodgates during storm surge events, which exert major morphodynamic control (Carniello et al., 2009, 2012). The reduction of water levels to mitigate the flood risk for the city of Venice and other urban settlements within the lagoon can trigger a series of hydrodynamic feedbacks, from the reduction of significant wave heights to the consequent increase in bottom shear stresses (Marani et al., 2015). A study conducted on the first trimester of Mo.S.E.'s operational activity highlighted that, although increased bottom shear stress over tidal flats leads to greater sediment remobilization, the redistribution of these sediments is significantly constrained by the low water levels in the lagoon. This effectively reduces the inorganic (mineral) deposition on salt marshes during storm-surge events which, though episodic, are critical for their vertical accretion (Tognin et al., 2021), while simultaneously promoting the infilling of channels (Tognin et al., 2022).

The critical role of tide regulation on the hydro- and morphodynamics of the lagoon requires a thorough understanding in the context of rising relative sea levels, which will necessitate increasingly frequent use of the barriers (Figure 22). This requires a more balanced application to ensure the safety of the city of Venice, along with the resilience of its ecosystems.

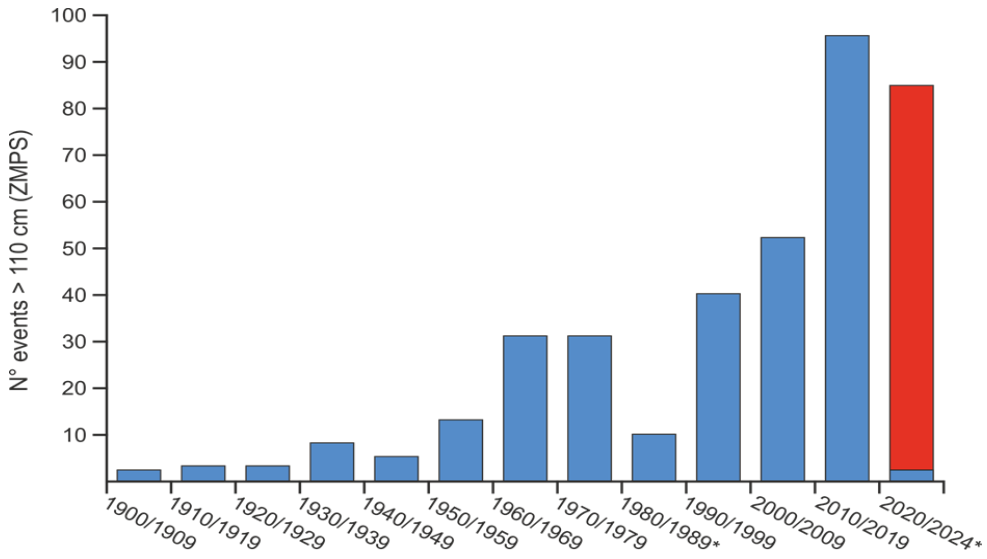

Figure 22. Decadal characterization of water levels (in blue) recorded in Venice that exceed the city's critical flood threshold, set at 1.10 m above the local reference datum of Punta della Salute (ZMPS). In red, the activation of the Mo.S.E. barriers to safeguard the city (starting from October 3rd, 2020). *Updated to 28/05/2024.

A two-dimensional (2D) model is employed, that consists of three modules, namely the hydrodynamic module coupled with the wind-wave module (WWTM) (Carniello et al., 2011) and the sediment transport and bed evolution module (STABEM) (Carniello et al., 2012) suitable for reproducing sediment dynamics governing the morphodynamic evolution of shallow micro-tidal basins.

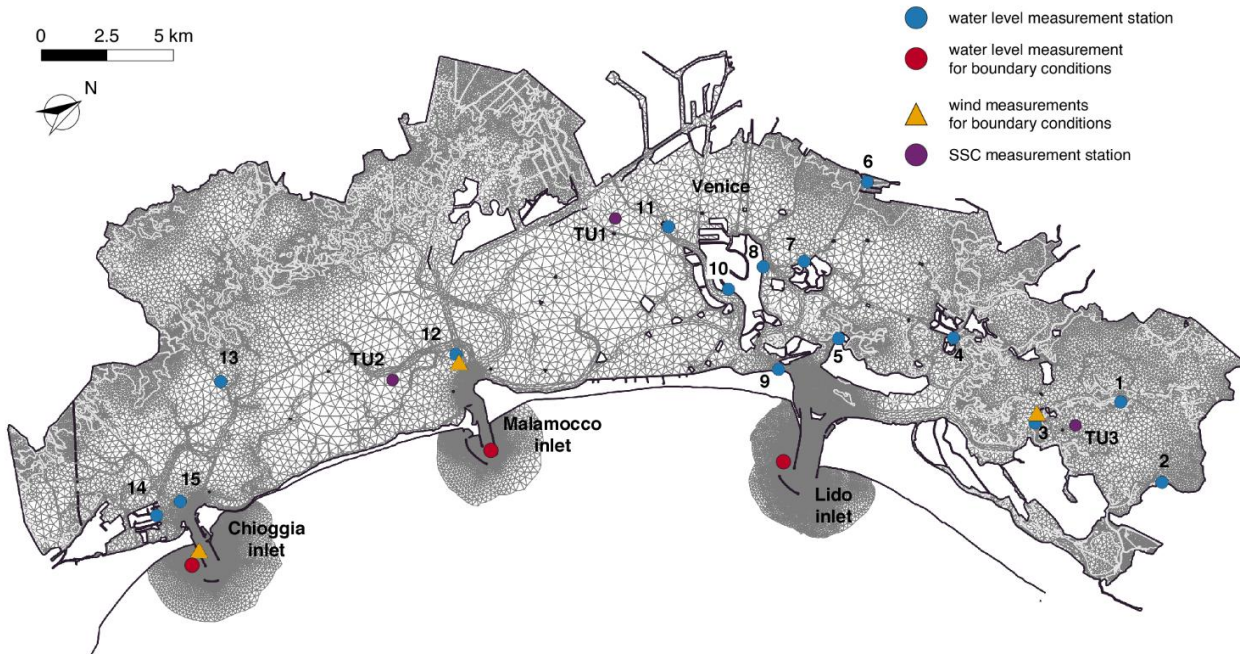

Figure 23. Computational grid. Blue circles indicate water level stations, whose measurements are used to test model results. Red circles indicate water level measurement stations adopted as boundary conditions. Orange triangles indicate wind measurement stations adopted as boundary conditions. Purple circles indicate suspended sediment concentration (SSC) measurement stations used to test model results.

The computational domain representing the Venice Lagoon (Figure 23) consists of 51084 nodes and 96751 triangular elements. The model is forced with water levels measured at the three inlets, as well as with wind directions and velocities measured in three different zones of the lagoon by the Venice Municipality "*Centro Previsioni e Segnalazioni Maree*" (CPSM) monitoring network (Figure 23).

5.4.1 Reliability of the hydrodynamic model

Previous insights (Carniello et al., 2005, 2011) demonstrated the ability of the numerical model to reproduce hydrodynamic processes driven by both tides and waves within the Lagoon of Venice. Additional testing of the model also proved its ability to accurately simulate hydrodynamic processes when the Mo.S.E. floodgates are activated (R. Mel et al., 2019; Tognin et al., 2022). A comparison between measured and modelled water levels for 15 different gauging stations within the Venice Lagoon is reported here (Figure 24 and Figure 25) for the first two-ever Mo.S.E. floodgate closures, occurred on October 3 and October 15, 2020. The hydrodynamic model accurately reproduces observed water levels, also under flood-regulated conditions.

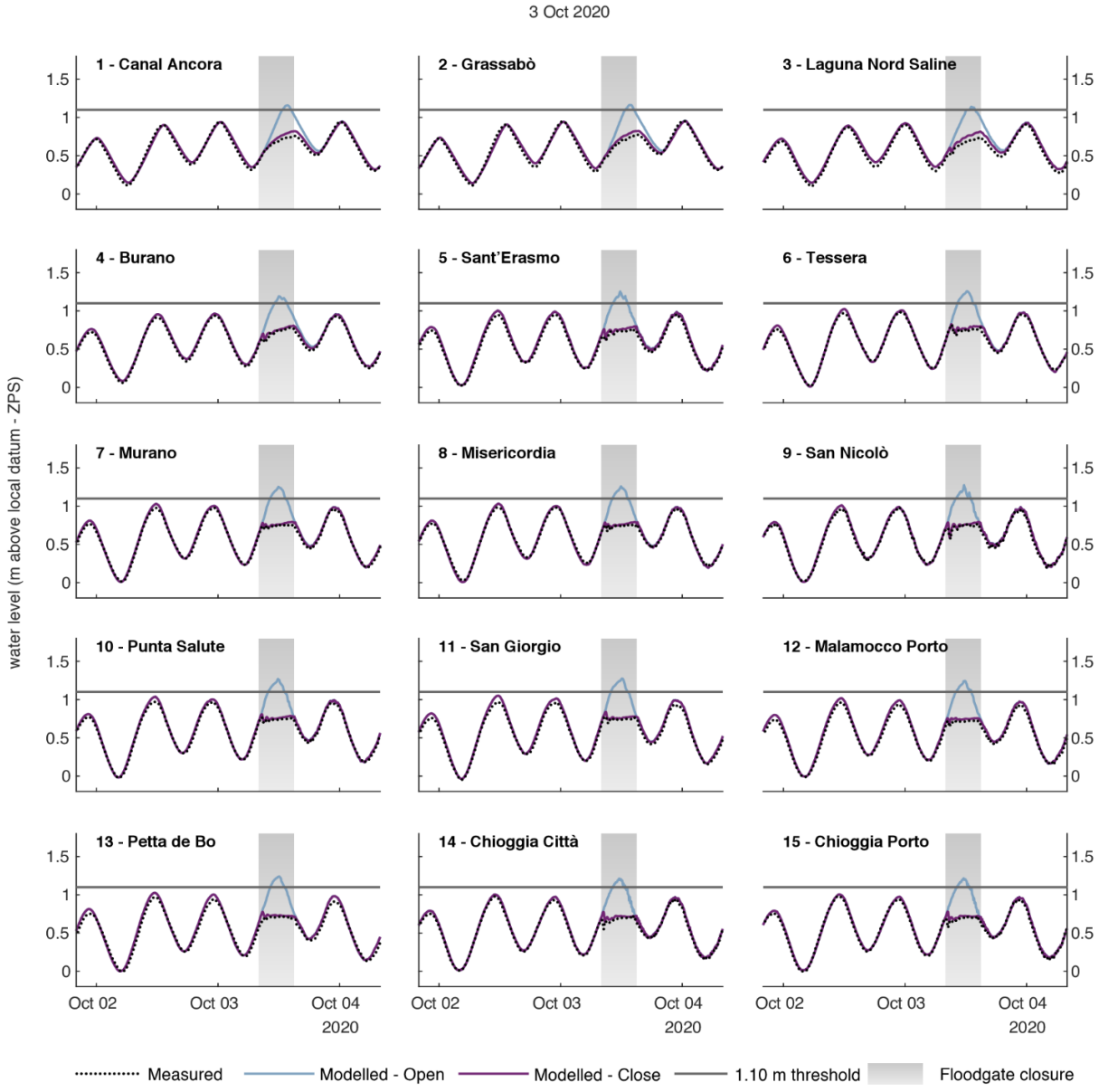

Figure 24: Water level for the 3 October event. Comparison between measured water level (black dots), modelled water level in the open barrier scenario (light blue), and modelled water level in the closed barrier scenario (purple).

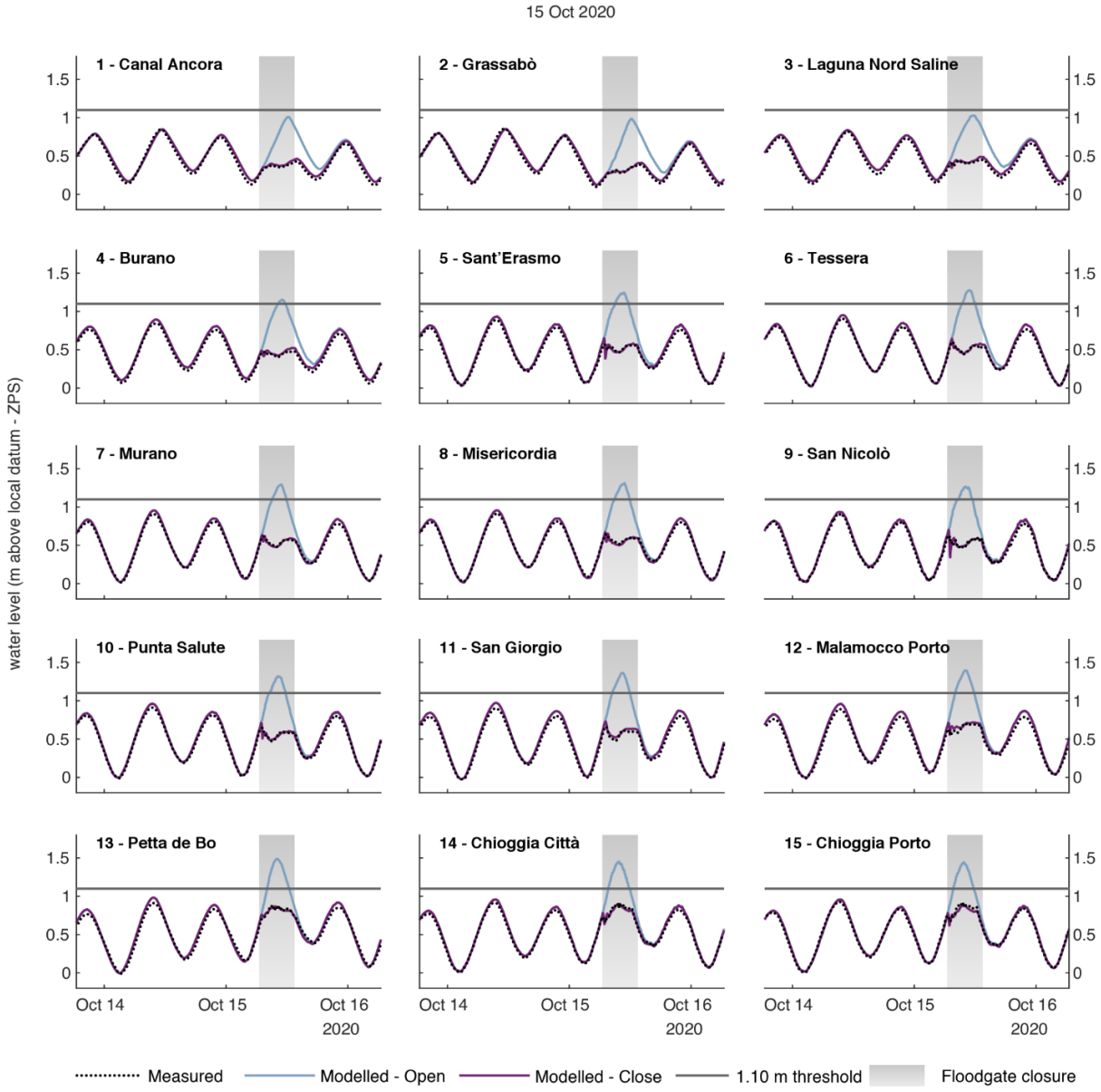

Figure 25: Water level for the 15 October event. Comparison between measured water level (black dots), modelled water level in the open barrier scenario (light blue), and modelled water level in the closed barrier scenario (purple).

Model reliability is quantified by means of standard statistical parameters, namely the Mean Absolute Error (MAE), Root Mean Squared Error (RMSE), and Nash-Sutcliffe Efficiency (NSE) (Table 3). MAE ranges between 0.016 and 0.043 m, RMSE is between 0.021 and 0.054 m. NSE is always higher than 0.94, thus the model performance is classified as "excellent" following the classification proposed by Allen et al. (2007).

Table 3: Model efficiency for water level. Model efficiency for water level computed in the 15 measurement stations shown in Figure 23 estimated through Mean Absolute Error (MAE), Root Mean Squared Error (RMSE) and Nash-Sutcliffe Efficiency (NSE), defined as $\mathbf{1} - \sum(\boldsymbol{d} - \boldsymbol{m})/\sum(\boldsymbol{d} - \boldsymbol{D})$, where d is the measured datum, m is the corresponding model estimate, and D is the mean of the measured data. Performance categories can be defined as follows: NSE >0.65 excellent (***); ME = 0.65–0.5 very good (**); ME = 0.5–0.2 good (**); ME <0.2 poor (*).

	Meas. Station	MAE		RMSE		NSE	
	Water level	3/10/2020	15/10/2020	3/10/2020	15/10/2020	3/10/2020	15/10/2020
1	Canal Ancora	0.035	0.035	0.050	0.050	0.952***	0.942***
2	Grassabò	0.037	0.034	0.053	0.054	0.946***	0.938***
3	Laguna Nord	0.042	0.038	0.050	0.046	0.950***	0.949***
4	Burano	0.029	0.036	0.036	0.040	0.979***	0.970***
5	Sant'Erasmo	0.033	0.029	0.037	0.034	0.980***	0.982***
6	Tessera	0.021	0.020	0.029	0.027	0.988***	0.989***
7	Murano	0.026	0.022	0.032	0.027	0.986***	0.989***
8	Misericordia	0.021	0.018	0.028	0.023	0.989***	0.992***
9	San Nicolò	0.024	0.023	0.030	0.031	0.988***	0.986***
10	Punta Salute	0.027	0.023	0.032	0.027	0.988***	0.990***
11	San Giorgio	0.038	0.037	0.044	0.042	0.977***	0.978***
12	Malamocco Porto	0.037	0.042	0.043	0.047	0.976***	0.970***
13	Petta de Bo	0.043	0.038	0.050	0.045	0.965***	0.977***
14	Chioggia Città	0.022	0.021	0.029	0.026	0.988***	0.991***
15	Chioggia Porto	0.022	0.017	0.028	0.021	0.988***	0.995***

5.4.2 Reliability of the sediment transport model

Previous insights (Carniello et al., 2012) demonstrated the ability of the numerical model to reproduce sediment transport processes at the temporal scale of individual tidal cycle within the Lagoon of Venice.
The ability of the model to reproduce sediment transport processes and the related bed evolution over longer timescale is evaluated here by comparing field measurements and model results in terms of suspended sediment concentration (SSC), as well as salt-marsh vertical accretion and tidal-flat bed elevation changes.

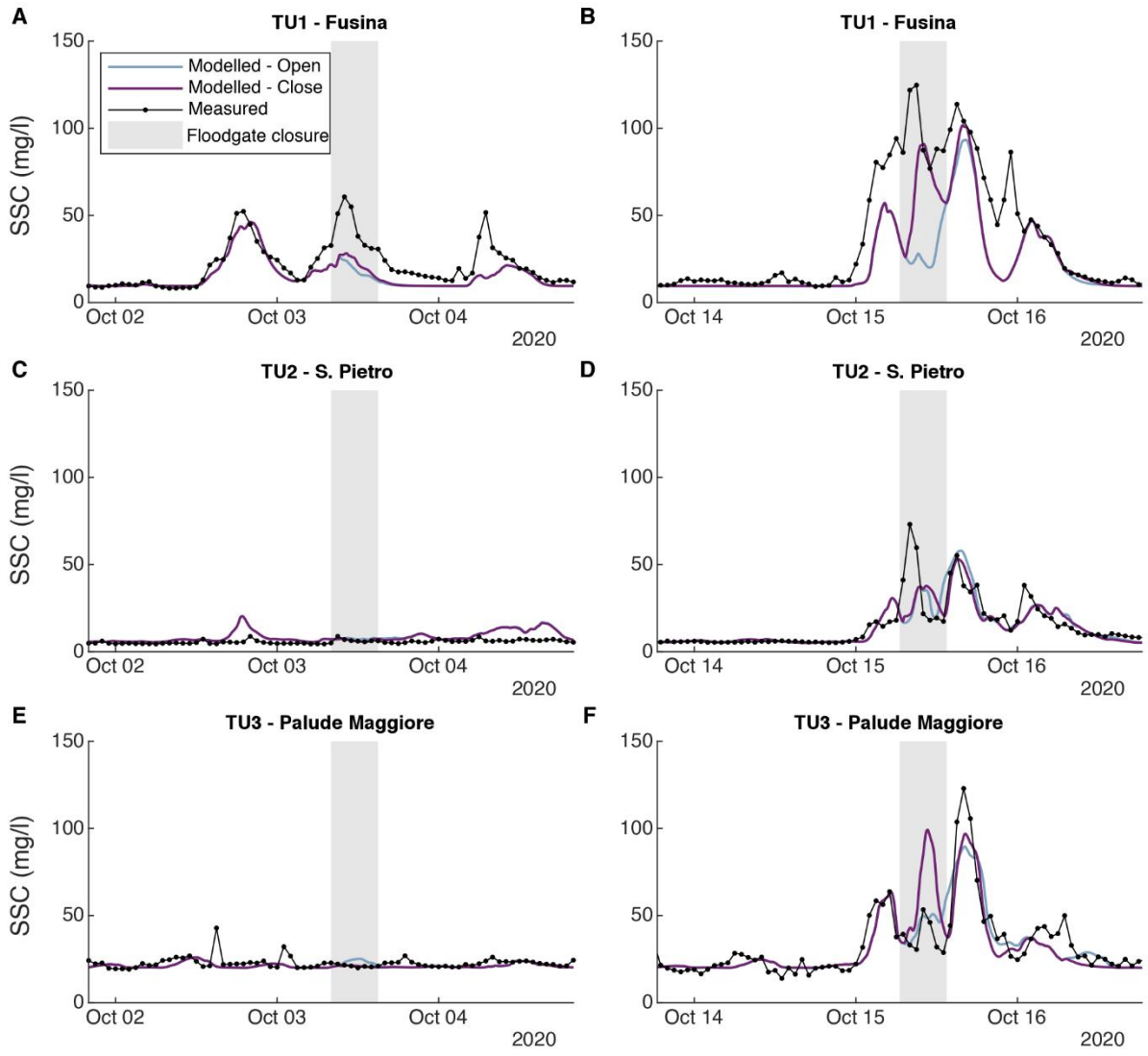

Figure 26: Suspended sediment concentration (SSC). Comparison between measured SSC (black line), modelled SSC in the open barrier scenario (light blue) and modelled SSC in the closed barrier scenario (purple). Measurement station positions are indicated in Figure 23. Notably, the model accurately predicts not only the magnitude of the SSC but also its modulation induced by tidal-level and wind-wave variations.

Figure 26 compares measured and modelled SSC during the 3 and 15 October closures at three different gauging stations within the lagoon (location shown in Figure 23), and the parameters to quantify model reliability are listed in Table 4. MAE is lower than 8.9 mg l^{-1} and RMSE is lower than 15.8 mg l^{-1}. The model efficiency is classified as “very good” based on NSE larger than 0.52 (Allen et al., 2007). Therefore, despite not begin as accurate as simulated water levels, modelled SSC values reasonably match measurements,

reproducing the magnitude and the modulation of SSC induced by the combined action of tidal levels and wind waves.

Table 4: Model efficiency for suspended sediment concentration (SSC). Model efficiency for SSC computed in the 3 measurement stations shown in Figure 26 estimated through Mean Absolute Error (MAE), Root Mean Squared Error (RMSE) and Nash-Sutcliffe Efficiency (NSE), defined as $\mathbf{1} - \sum(\boldsymbol{d} - \boldsymbol{m})/\sum(\boldsymbol{d} - \boldsymbol{D})$, where d is the measured datum, m is the corresponding model estimate, and D is the mean of the measured data. Performance categories can be defined as follows: NSE >0.65 excellent (***); ME = 0.65–0.5 very good (**); ME = 0.5–0.2 good (**); ME <0.2 poor (*).

	Meas. Station	MAE		RMSE		NSE	
	SSC	3/10/2020	15/10/2020	3/10/2020	15/10/2020	3/10/2020	15/10/2020
1	TU1 - Fusina	4.790	8.914	6.526	15.879	0.525**	0.638**
2	TU2 – S.Pietro	1.162	3.466	1.537	7.238	0.557**	0.607**
3	TU3 – Palude Maggiore	1.598	6.039	1.957	11.389	0.535**	0.542**

Salt-marsh accretion measurements are available for 27 sites grouped in three marshes (locations shown in the upper panel of Figure 27). Accretion was measured through kaolinite horizon markers and yearly accretion rates are available for the period 2019-2020 (Tognin et al., 2021). To compare field measurements and model results, *ad hoc* numerical simulations were performed using water levels and wind climate measured during the observation period as boundary conditions. The comparison between field measurements and model results is performed both at the scale of individual marshes and for the whole lagoon (Figure 27). The non-parametric Kolgomorov-Smirnov test is used to quantitatively compare the distributions of measured and modelled accretion rates and it confirms that they do not significantly differ (significance level $\alpha = 0.01$) for each considered study site as well as for the whole lagoon (Table 5).

Table 5: Statistical test on salt-marsh accretion. Results of the Kolmogorov-Smirnov test performed to test the null hypothesis that measured and modelled salt-marsh accretion rate are from the same distribution. h = 0 indicates that the test does not reject the null hypothesis, and h = 1 otherwise. Significance level $\boldsymbol{\alpha = 0.01}$.

	Area	h	p-value
1	CO	0	0.708
2	SE	0	0.065
3	SF	0	0.387
4	Lagoon	0	0.724

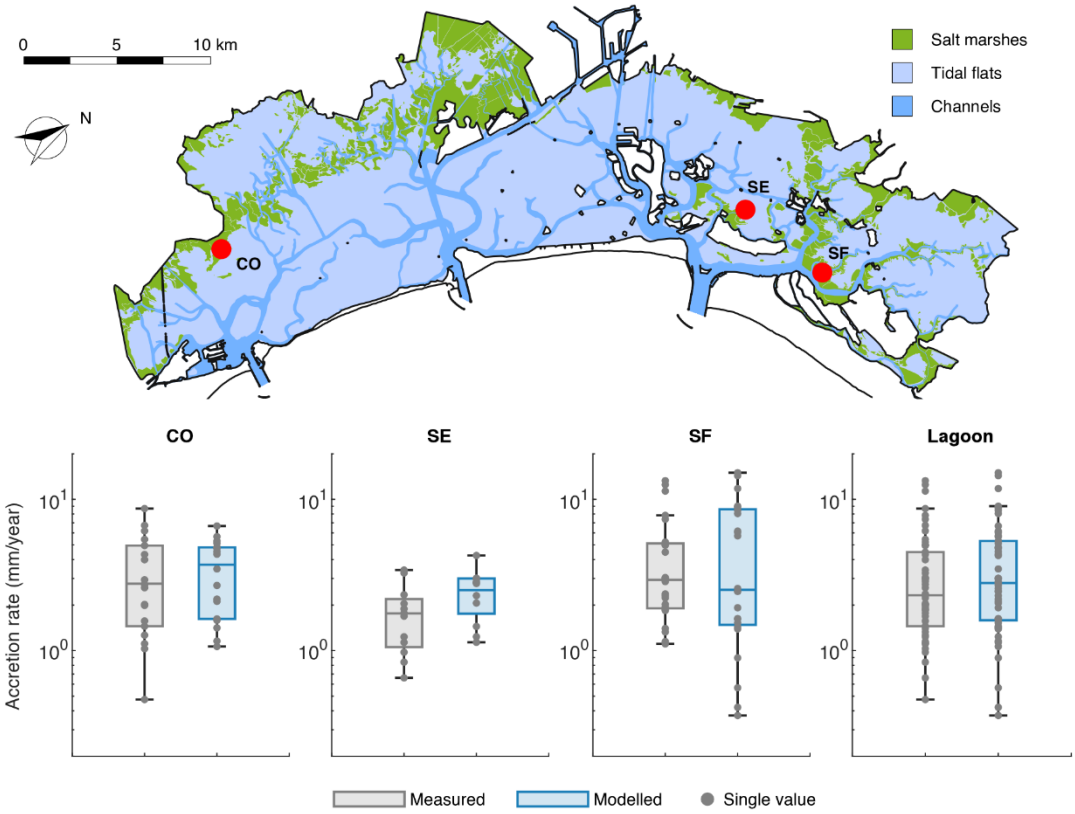

Figure 27: Comparison between measured and modelled salt-marsh accretion. Comparison between measured (grey) and modelled (blue) accretion rates on salt marshes. Data refer to years 2019 and 2020. Locations of the marsh study sites are shown by red dots in the upper panel. All y-axes in the lower panels are on a logarithmic scale.

Although direct measurements of bed elevation change on tidal flats are not available, estimates of erosion and deposition rates can be obtained from periodic bathymetric surveys available at the scale of the entire lagoon. In particular, we computed the mean annual bed elevation change experienced by tidal flats of the Venice Lagoon by subtracting the digital elevation model derived from the two most recent bathymetries available (i.e., 1970 and 2003) and by computing the mean rate of change. We then compared the results with the annual bed elevation change computed through the numerical model using water levels and wind climate measured in 2005 and 2020 as boundary conditions. The year 2005 is selected because probability distributions of water levels and wind conditions are closest to median values for the period 2000-2020, and thus morphological changes obtained with these forcing factors are deemed to be similar to those experienced by the lagoon over decadal timescales and captured by bathymetric surveys. Despite being characterized by water levels and wind conditions different from the average, numerical simulations are performed for the year 2020 as well, as it represents the year in which the Mo.S.E. barrier system became operational.

Modelled and observed bed elevation changes are compared for 20 tidal-flat sites (circular areas with radius equal to 1 km) distributed all over the Venice Lagoon (locations shown in the upper panel of Figure 28). Boxplots in Figure 28 show that bed elevation changes retrieved from bathymetric data are comparable with those computed using the numerical model, both for the 2005 and 2020 simulations. Kolmogorov-Smirnov tests show that model results of the 2005 simulation do not significantly differ from bathymetric measurements

in any case (significance level α = 0.01, Table 6). In addition, bed elevation changes resulting from the 2020 simulation do not significantly differ from field data in 16 out of the 20 study sites (α = 0.01, Table 6).

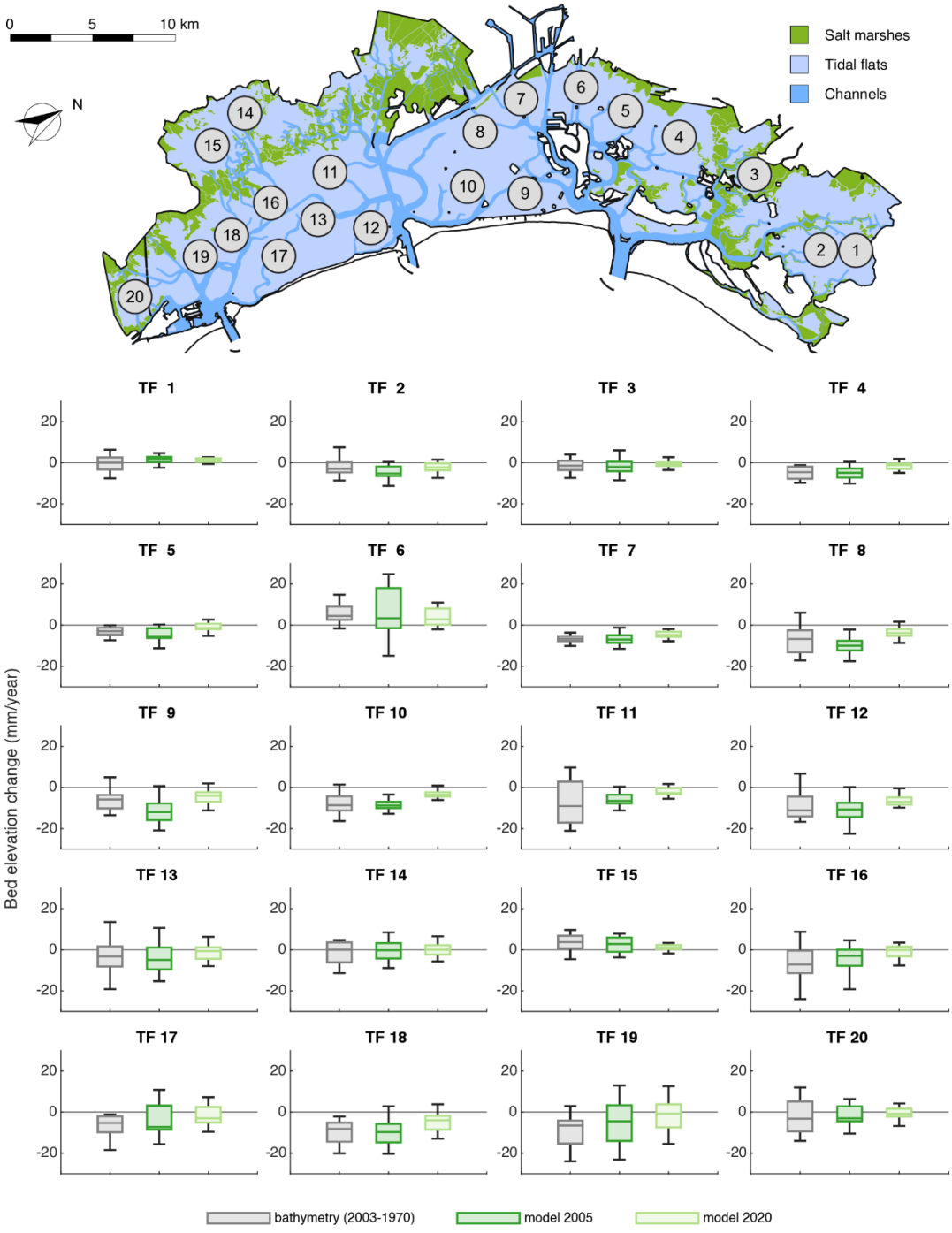

Figure 28: Comparison between measured and modelled bed elevation change on tidal flats. Comparison between bed elevation change obtained from bathymetric surveys (grey) and modelled using as boundary conditions water levels and wind climate measured in 2005 (dark green) and 2020 (light green). Locations of the studied tidal flat areas are shown in the upper panel.

Table 6: Statistical test on tidal-flat bed elevation change. Results of the Kolmogorov-Smirnov test performed to test the null hypothesis that measured and modelled tidal-flat bed elevation change are from the same distribution. The test compares the bed elevation change obtained from bathymetric surveys with model results obtained using as boundary conditions water level and wind climate measured in 2005 (3rd and 4th columns) and 2020 (5th and 6th columns). h = 0 indicates that the test does not reject the null hypothesis, and h = 1 otherwise. Significance level $\boldsymbol{\alpha = 0.01}$.

		Bathymetry – Mod. 2005		Bathymetry – Mod. 2020	
	Area	h	p-value	h	p-value
1	TF 1	0	0.247	0	0.116
2	TF 2	0	0.218	0	0.709
3	TF 3	0	0.999	0	0.247
4	TF 4	0	0.018	1	0.002
5	TF 5	0	0.190	0	0.031
6	TF 6	0	0.247	0	0.247
7	TF 7	0	0.012	1	0.001
8	TF 8	0	0.116	0	0.049
9	TF 9	0	0.018	0	0.116
10	TF 10	0	0.060	1	4.22E-06
11	TF 11	0	0.059	1	1.83E-04
12	TF 12	0	0.742	1	0.006
13	TF 13	0	0.956	0	0.462
14	TF 14	0	0.945	0	0.425
15	TF 15	0	0.425	1	0.001
16	TF 16	0	0.387	0	0.031
17	TF 17	0	0.673	0	0.190
18	TF 18	0	0.965	0	0.059
19	TF 19	0	0.425	0	0.014
20	TF 20	0	0.010	0	0.010

The statistical comparison between field measurements and model results in terms of SSC, salt-marsh accretion, and bed elevation changes of tidal flats shows that erosional and depositional fluxes, together with

the resulting elevation changes of different morphological units, are reasonably captured by the numerical model.

6. References

Alesheikh, A. A., Ghorbanali, A., & Nouri, N. (2007). Coastline change detection using remote sensing. International Journal of Environmental Science & Technology, 4(1), 61–66.

Allen, J. I., Somerfield, P. J., & Gilbert, F. J. (2007). Quantifying uncertainty in high-resolution coupled hydrodynamic-ecosystem models. Journal of Marine Systems, 64(1–4), 3–14. https://doi.org/10.1016/j.jmarsys.2006.02.010

Amos, C. L., Umgiesser, G., Tosi, L., & Townend, I. H. (2010). The coastal morphodynamics of Venice lagoon, Italy: An introduction. Continental Shelf Research, 30(8), 837–846. https://doi.org/10.1016/j.csr.2010.01.014

Antonioli, F., De Falco, G., Lo Presti, V., Moretti, L., Scardino, G., Anzidei, M., ... & Mastronuzzi, G. (2020). Relative sea-level rise and potential submersion risk for 2100 on 16 coastal plains of the Mediterranean sea. Water, 12(8), 2173.

Baldoni, A., Perugini, E., Penna, P., Parlagreco, L. & Brocchini, M. (2022). A comprehensive study of the river plume in a microtidal setting. Estuarine, Coastal and Shelf Science, 275, 107995.

Baldoni, A., Perugini, E., Soldini, L., Calantoni, J. & Brocchini, M. (2021). Long-term evolution of an inner bar at the mouth of a microtidal river. Estuarine, Coastal and Shelf Science, 262, 107573.

Baldoni, A., (2023). Observation and modeling of the estuarine and coastal hydro-morphodynamics: the Misa River case study. PhD thesis. Università Politecnica delle Marche. https://hdl.handle.net/11566/315068

Bayram, B., Janpaule, I., Avşar, Ö., Oğurlu, M., Bozkurt, S., Çatal Reis, H., & Zafer Şeker, D. (2015). Shoreline Extraction and Change Detection using 1:5000 Scale Orthophoto Maps: A Case Study of Latvia-Riga. Journal, 2(3), 1–6.

Barausse, A., Grechi, L., Martinello, N., Musner, T., Smania, D., Zangaglia, A., & Palmeri, L. (2015). An integrated approach to prevent the erosion of salt marshes in the lagoon of Venice. EQA - International Journal of Environmental Quality, 18(1), 43–54. https://doi.org/10.6092/issn.2281-4485/5799

Bárcena, J. F., Camus, P., García, A., & Álvarez, C. (2015). Selecting model scenarios of real hydrodynamic forcings on mesotidal and macrotidal estuaries influenced by river discharges using K-means clustering. Environmental Modelling & Software, 68, 70-82.

Boccotti, P., 2004. Idraulica marittima. UTET Università

Booij, N., Holthuijsen, L., Ris, R., 1996. The" swan" wave model for shallow water, in: Coastal Engineering 1996, pp. 668–676

Booij, N. R. R. C., Ris, R. C., and Holthuijsen, L. H. (1999). A third-generation wave model for coastal regions: 1. Model description and validation. J. Geophys. Res. Oceans 104, 7649–7666. doi: 10.1029/98JC02622

Booij, N., Haagsma, I. G., Holthuijsen, L. A., Kieftenburg, A. T., Ris, R. C., vd Westhuysen, A. J., & Zijlema, M. (2004). Swan user manual, swan cycle iii version 40.41. Delft: Delft University of Technology.

Breda, A., Saco, P. M., Sandi, S. G., Saintilan, N., Riccardi, G., & Rodríguez, J. F. (2021). Accretion, retreat and transgression of coastal wetlands experiencing sea-level rise. Hydrology and Earth System Sciences, 25(2), 769–786. https://doi.org/10.5194/hess-25-769-2021

Brocchini, M., Calantoni, J., Postacchini, M., Sheremet, A., Staples, T., Smith, J., Reed, A. H., Braithwaite III, E. F., Lorenzoni, C., Russo, A., Corvaro, S., Mancinelli, A. & Soldini, L. (2017). Comparison between the wintertime and summertime dynamics of the Misa River estuary. Marine Geology, 385, 27-40.

Camus, P., Mendez, F. J., Medina, R., & Cofiño, A. S. (2011). Analysis of clustering and selection algorithms for the study of multivariate wave climate. Coastal Engineering, 58(6), 453-462.

Camus, P., Mendez, F. J., & Medina, R. (2011b). A hybrid efficient method to downscale wave climate to coastal areas. Coastal Engineering, 58(9), 851-862.

Carbognin, L., Teatini, P., & Tosi, L. (2004). Eustacy and land subsidence in the Venice Lagoon at the beginning of the new millennium. Journal of Marine Systems, 51(1-4 SPEC. ISS.), 345–353. https://doi.org/10.1016/j.jmarsys.2004.05.021

Carniello, L., Defina, A., Fagherazzi, S., & D'Alpaos, L. (2005). A combined wind wave-tidal model for the Venice lagoon, Italy. Journal of Geophysical Research: Earth Surface, 110(4), 1–15. https://doi.org/10.1029/2004JF000232

Carniello, L., Defina, A., & D'Alpaos, L. (2009). Morphological evolution of the Venice lagoon: Evidence from the past and trend for the future. Journal of Geophysical Research: Earth Surface, 114(4), 1–10. https://doi.org/10.1029/2008JF001157

Carniello, L., D'Alpaos, A., & Defina, A. (2011). Modeling wind waves and tidal flows in shallow micro-tidal basins. Estuarine, Coastal and Shelf Science, 92(2), 263–276. https://doi.org/10.1016/j.ecss.2011.01.001

Carniello, L., Defina, A., & D'Alpaos, L. (2012). Modeling sand-mud transport induced by tidal currents and wind waves in shallow microtidal basins: Application to the Venice Lagoon (Italy). Estuarine, Coastal and Shelf Science, 102–103, 105–115. https://doi.org/10.1016/j.ecss.2012.03.016

Carniello, L., Silvestri, S., Marani, M., D'Alpaos, A., Volpe, V., & Defina, A. (2014). Sediment dynamics in shallow tidal basins: In situ observations, satellite retrievals, and numerical modeling in the Venice Lagoon. Journal of Geophysical Research: Earth Surface, 119(4), 802–815. https://doi.org/10.1002/2013JF003015

Caires, S., & Yan, K. (2020). Ocean surface wave time series for the European coast from 1976 to 2100 derived from climate projections. Copernicus Climate Change Service (C3S) Climate Data Store (CDS).

Consorzio di Bonifica delle Marche. Porto di Senigallia – Studio modellistico a supporto della progettazione di un'opera marittima a protezione del canale terminale del fiume Misa a Senigallia (AN) (2020).

D'Alpaos, A., Carniello, L., & Rinaldo, A. (2013). Statistical mechanics of wind wave-induced erosion in shallow tidal basins: Inferences from the Venice Lagoon. Geophysical Research Letters, 40(13), 3402–3407. https://doi.org/10.1002/grl.50666

D'Alpaos, L. (2010). Fatti e misfatti di idraulica lagunare. La laguna di Venezia dalla diversione dei fiumi alle nuove opere delle bocche di porto. (L D'Alpaos, Ed.), Istituto Veneto di Scienze, Lettere e Arti (Vol. 1999). Venice: Istituto Veneto di Scienze, Lettere ed Arti.

Dangendorf, S., Frederikse, T., Chafik, L., Klinck, J. M., Ezer, T., & Hamlington, B. D. (2021). Data-driven reconstruction reveals large-scale ocean circulation control on coastal sea level. Nature Climate Change, 11(6), 514-520.

De Goede, E. D. (2020). Historical overview of 2D and 3D hydrodynamic modelling of shallow water flows in the Netherlands. Ocean Dynamics, 70(4), 521-539.

Defina, A. (2000). Two-dimensional shallow flow equations for partially dry areas. Water Resources Research, 36(11), 3251–3264. https://doi.org/10.1029/2000WR900167

Enríquez, A. R., Wahl, T., Marcos, M., & Haigh, I. D. (2020). Spatial footprints of storm surges along the global coastlines. Journal of Geophysical Research: Oceans, 125(9).

Fernández-Montblanc, T., Duo, E., Ciavola, P., 2020. Dune reconstruction and revegetation as a potential measure to decrease coastal erosion and flooding under extreme storm conditions. Ocean & Coastal Management 188, 10507

Ferrarin, C., Tomasin, A., Bajo, M., Petrizzo, A., & Umgiesser, G. (2015). Tidal changes in a heavily modified coastal wetland. Continental Shelf Research, 101, 22–33. https://doi.org/10.1016/j.csr.2015.04.002

Fox-Kemper, B., Hewitt, H., Xiao, C., Aðalgeirsdóttir, G., Drijfhout, S., Edwards, T., Golledge, N., Hemer, M., Kopp, R., Krinner, G., Mix, A., Notz, D., Nowicki, S., Nurhati, I., Ruiz, L., Sallée, J.B., Slangen, A., Yu, Y., 2021. Ocean, Cryosphere and Sea Level Change. Cambridge University Press, Cambridge, United Kingdom and New York, NY, USA. pp. 1211–1362.

Finotello, A., Canestrelli, A., Carniello, L., Ghinassi, M., & D'Alpaos, A. (2019). Tidal Flow Asymmetry and Discharge of Lateral Tributaries Drive the Evolution of a Microtidal Meander in the Venice Lagoon (Italy). Journal of Geophysical Research: Earth Surface, 124(12), 3043–3066. https://doi.org/10.1029/2019JF005193

Finotello, A., Marani, M., Carniello, L., Pivato, M., Roner, M., Tommasini, L., & D'alpaos, A. (2020). Control of wind-wave power on morphological shape of salt marsh margins. Water Science and Engineering, 13(1), 45–56. https://doi.org/10.1016/j.wse.2020.03.006

Finotello, A., Capperucci, R. M., Bartholomä, A., D'Alpaos, A., & Ghinassi, M. (2022). Morpho-sedimentary evolution of a microtidal meandering channel driven by 130 years of natural and anthropogenic modifications of the Venice Lagoon (Italy). Earth Surface Processes and Landforms, 47(10), 2580–2596. https://doi.org/10.1002/esp.5396

Frignani, M., Langone, L., Ravaioli, M., Sorgente, D., Alvisi, F., & Albertazzi, S. (2005). Fine- sediment mass balance in the western Adriatic continental shelf over a century time scale. Mar. Geol. 222, 113–133.

Garzon, J.L., Maza, M., Ferreira, C., Lara, J., Losada, I., 2019. Wave attenuation by spartina saltmarshes in the chesapeake bay under storm surge conditions. Journal of Geophysical Research: Oceans 124, 5220–5243.

Gatto, P., & Carbognin, L. (1981). The lagoon of venice: Natural environmental trend and man-induced modification. Hydrological Sciences Bulletin, 26(4), 379–391. https://doi.org/10.1080/02626668109490902

Ghezzo, M., Guerzoni, S., Cucco, A., & Umgiesser, G. (2010). Changes in Venice Lagoon dynamics due to construction of mobile barriers. Coastal Engineering, 57(7), 694–708. https://doi.org/10.1016/j.coastaleng.2010.02.009

Hennig, C., Meila, M., Murtagh, F., & Rocci, R. (2015). Handbook of cluster analysis. Boca Raton: CRC press.

Holthuijsen, L. H., Booij, N., & Herbers, T. H. C. (1989). A prediction model for stationary, short-crested waves in shallow water with ambient currents. Coastal Engineering, 13(1), 23–54. https://doi.org/10.1016/0378-3839(89)90031-8

Korres, G., Ravdas, M., & Zacharioudaki, A. (2019). Mediterranean sea waves analysis and forecast (CMEMS MED-Waves).

Knutson, P.L., Brochu, R.A., Seelig, W.N., Inskeep, M., 1982. Wave damping in spartina alterniflora marshes. Wetlands 2, 87–104

Leonardi, N., Ganju, N. K., & Fagherazzi, S. (2016). A linear relationship between wave power and erosion determines salt-marsh resilience to violent storms and hurricanes. Proceedings of the National Academy of Sciences of the United States of America, 113(1), 64–68. https://doi.org/10.1073/pnas.1510095112

Losada, I. J., Toimil, A., Munoz, A., Garcia-Fletcher, A. P., & Diaz-Simal, P. (2019). A planning strategy for the adaptation of coastal areas to climate change: The Spanish case. Ocean & coastal management, 182, 104983.

Li, C., Wang, H., Liao, X., Xiao, R., Liu, K., Bai, J., & He, Q. (2022). Heavy metal pollution in coastal wetlands: A systematic review of studies globally over the past three decades. Journal of Hazardous Materials, 424, 127312.

Manning, A.J., Baugh, J.V., Spearman, J.R., Pidduck, E.L., Whitehouse, R.J.S., 2011. The settling dynamics of flocculating mud:sand mixtures: Part 1 – empirical algorithm development. In: Ocean Dynamics, INTERCOH 2009 special issue. https://doi.org/ 10.1007/s10236-011-0394-7.

Marani, M., D'alpaos, A., Lanzoni, S., & Santalucia, M. (2011). Understanding and predicting wave erosion of marsh edges. Geophysical Research Letters, 38(21), 1–5. https://doi.org/10.1029/2011GL048995

MARINO, M., MUSUMECI, R. E., CAVALLARO, L., & FOTI, E. (2023). ASSESSMENT OF COASTAL RESTORATION MEASURES TO MITIGATE COASTAL FLOODING IN A CONTEXT OF CLIMATE CHANGE: THE CASE OF THE SOUTH-EAST OF SICILY LAGOONS. In Coastal Sediments 2023: The Proceedings of the Coastal Sediments 2023 (pp. 2286-2292).

Mariotti, G., & Fagherazzi, S. (2013). Critical width of tidal flats triggers marsh collapse in the absence of sea-level rise. Proceedings of the National Academy of Sciences of the United States of America, 110(14), 5353–5356. https://doi.org/10.1073/pnas.1219600110

Mariotti, G., Fagherazzi, S., Wiberg, P. L., McGlathery, K. J., Carniello, L., & Defina, A. (2010). Influence of storm surges and sea level on shallow tidal basin erosive processes. Journal of Geophysical Research: Oceans, 115(11), 1–17. https://doi.org/10.1029/2009JC005892

Matticchio, B., Carniello, L., Canesso, D., Ziggiotto, E., & Cordella, M. (2017). Recent changes in tidal propagation in the Venice Lagoon: effects of changes in the inlet structure. In Luigi D'Alpaos (Ed.), Commissione di studio sui problemi di Venezia, Volume III: La laguna di Venezia e le nuove opere alle bocche (Istituto V, pp. 157–183). Venice: Istituto Veneto di Scienze, Lettere ed Arti.

Mehta, A. J., Hayter, E. J., Parker, W. R., Krone, R. B., & Teeter, A. M. (1989). Cohesive Sediment Transport. I: Process Description. Journal of Hydraulic Engineering, 115(8), 1076–1093. https://doi.org/10.1061/(asce)0733-9429(1989)115:8(1076)

McLaughlin, C. J., Smith, C. A., Buddemeier, R. W., Bartley, J. D., & Maxwell, B. A. (2003). Rivers, runoff, and reefs. Global and Planetary Change, 39(1-2), 191-199.

Mel, R., Carniello, L., & D'Alpaos, L. (2019). Addressing the effect of the Mo.S.E. barriers closure on wind setup within the Venice lagoon. Estuarine, Coastal and Shelf Science, 225(January), 106249. https://doi.org/10.1016/j.ecss.2019.106249

Mel, R. A., Viero, D. Pietro, Carniello, L., Defina, A., & D'Alpaos, L. (2021). The first operations of Mo.S.E. system to prevent the flooding of Venice: Insights on the hydrodynamics of a regulated lagoon. Estuarine, Coastal and Shelf Science, 261(August), 107547. https://doi.org/10.1016/j.ecss.2021.107547

Melito, L., Parlagreco, L., Perugini, E., Postacchini, M., Devoti, S., Soldini, L., ... & Brocchini, M. (2020). Sandbar dynamics in microtidal environments: Migration patterns in unprotected and bounded beaches. Coastal Engineering, 161, 103768.

Milliman, J.D. & Syvitski, J.P. (1992). Geomorphic/tectonic control of sediment discharge to the ocean: the importance of small mountainous rivers. J. Geol. 100 (5), 525–544.

Mohamed, B., Abdallah, A. M., Alam El-Din, K., Nagy, H., & Shaltout, M. (2019). Inter-annual variability and trends of sea level and sea surface temperature in the Mediterranean Sea over the last 25 years. Pure and Applied Geophysics, 176, 3787-3810.

Möller, I., Spencer, T., French, J. R., Leggett, D. J., & Dixon, M. (1999). Wave transformation over salt marshes: A field and numerical modelling study from north Norfolk, England. Estuarine, Coastal and Shelf Science, 49(3), 411–426. https://doi.org/10.1006/ecss.1999.0509

Musumeci, R. E., Marino, M., Cavallaro, L., & Foti, E. (2023). DOES COASTAL WETLAND RESTORATION WORK AS A CLIMATE CHANGE ADAPTATION STRATEGY? THE CASE OF THE SOUTH-EAST OF SICILY COAST. Coastal Engineering Proceedings, (37), papers.66. https://doi.org/10.9753/icce.v37.papers.66

NASA Sea Level Change Portal, Accessed: 2024. IPCC AR6 Sea Level Projection Tool. https://sealevel.nasa.gov/ipcc-ar6-sea-level-projection-tool.

Oo, Y. H., Da Silva, G. V., Zhang, H., Strauss, D., & Tomlinson, R. (2022). Estimation of beach erosion using Joint Probability analysis with a morphological model. Ocean Engineering, 264, 112560.

Parker, G., Garcia, M., Fukushima, Y., & Yu, W. (1987). Experiments on turbidity currents over an erodible bed. Journal of Hydraulic Research, 25(1), 123–147. https://doi.org/10.1080/00221688709499292

Postacchini, M., Soldini, L., Lorenzoni, C., & Mancinelli, A. (2017). Medium-term dynamics of a middle Adriatic barred beach. Ocean Science, 13(5), 719-734.

Postacchini, M., Lalli, F., Memmola, F., Bruschi, A., Bellafiore, D., Lisi, I., ... & Brocchini, M. (2019). A model chain approach for coastal inundation: Application to the bay of Alghero. Estuarine, Coastal and Shelf Science, 219, 56-70.

Postacchini, M., Manning, A. J., Calantoni, J., Smith, J. P., & Brocchini, M. (2023). A storm driven turbidity maximum in a microtidal estuary. Estuarine, Coastal and Shelf Science, 288, 108350.

Reddy, C. K., & Vinzamuri, B. (2018). A survey of partitional and hierarchical clustering algorithms. In C. K. Reddy, & B. Vinzamuri, Data clustering (p. 87-110). : Chapman and Hall/CRC.

Riahi, K., Van Vuuren, D.P., Kriegler, E., Edmonds, J., O'neill, B.C., Fujimori, S., Bauer, N., Calvin, K., Dellink, R., Fricko, O., et al., 2017. The shared socioeconomic pathways and their energy, land use, and greenhouse gas emissions implications: An overview. Global environmental change 42, 153–168

Roelvink, D., Reniers, A., Van Dongeren, A., De Vries, J.V.T., McCall, R., Lescinski, J., 2009. Modelling storm impacts on beaches, dunes and barrier islands. Coastal engineering 56, 1133–1152

Roelvink, D., Reniers, A. J., Van Dongeren, A. P., Van Thiel de Vries, J., Lescinski, J., & McCall, R. (2010). XBeach model description and manual. Delft: Unesco-IHE Institute for Water Education, Deltares and Delft University of Tecnhology.

Rogers, W. E. (2020). Phase-averaged wave models. Ocean Wave Dynamics, 336, 163-204.

Shi, F., Kirby, J. T., Harris, J. C., Geiman, J. D., and Grilli, S. T. (2012). A high-order adaptive time-stepping TVD solver for Boussinesq modeling of breaking waves and coastal inundation. Ocean Modelling 43, 36–51. doi: 10.1016/j.ocemod.2011.12.004

Silvestri, S., D'Alpaos, A., Nordio, G., & Carniello, L. (2018). Anthropogenic Modifications Can Significantly Influence the Local Mean Sea Level and Affect the Survival of Salt Marshes in Shallow Tidal Systems. Journal of Geophysical Research: Earth Surface, 123(5), 996–1012. https://doi.org/10.1029/2017JF004503

Smagorinsky, J. (1963). General Circulation Experiments With the Primitive Equations. Monthly Weather Review, 91(3), 99–164. https://doi.org/10.1175/1520-0493(1963)091<0099:gcewtp>2.3.co;2

Soulsby, R. L. (1995). Bed shear-stresses due to combined waves and currents. In M. J. F. et al Stive (Ed.), Advanced in Coastal Morphodynamics (pp. 20–23). Delft Hydraul., Delft, Netherlands.

Tagliapietra, D., Baldan, D., Barausse, A., Buosi, A., Curiel, D., Guarneri, I., et al. (2018). Protecting and restoring the salt marshes and seagrasses in the lagoon of Venice. In X. D. Quintana, D. Boix, S. Gascòn, & J. Sala (Eds.), Management and Restoration of Mediterranean Coastal Lagoons in Europe. Included in the Project "LIFE Pletera (LIFE13 NAT/ES/001001) (Càtedra d', p. 220). Venice, Italy: Càtedra d'Ecosistemes Litorals Mediterrànis i LIFE Pletera. Retrieved from http://lifepletera.com/wp-content/uploads/2019/02/Recerca_i_Territori_10_ENG_MdM_web.pdf

Temmerman, S., Bouma, T. J., Govers, G., Wang, Z. B., De Vries, M. B., & Herman, P. M. J. (2005). Impact of vegetation on flow routing and sedimentation patterns: Three-dimensional modeling for a tidal marsh. Journal of Geophysical Research: Earth Surface, 110(4), 1–18. https://doi.org/10.1029/2005JF000301

Tognin, D., D'Alpaos, A., Marani, M., & Carniello, L. (2021). Marsh resilience to sea-level rise reduced by storm-surge barriers in the Venice Lagoon. Nature Geoscience, 14(12), 906–911. https://doi.org/10.1038/s41561-021-00853-7

Tognin, D., Finotello, A., D'Alpaos, A., Viero, D. Pietro, Pivato, M., Mel, R. A., et al. (2022). Loss of geomorphic diversity in shallow tidal embayments promoted by storm-surge barriers. Science Advances, 8(13), 1–13. https://doi.org/10.1126/sciadv.abm8446

Tomasin, A. (1974). Recent changes in the tidal regime in Venice. Rivista Italiana Geofisica, 23(5/6), 275–278.

Tommasini, L., Carniello, L., Ghinassi, M., Roner, M., & D'Alpaos, A. (2019). Changes in the wind-wave field and related salt-marsh lateral erosion: inferences from the evolution of the Venice Lagoon in the last four centuries. Earth Surface Processes and Landforms, 44(8), 1633–1646. https://doi.org/10.1002/esp.4599

Valle-levinson, A., Marani, M., Carniello, L., Alpaos, A. D., Lanzoni, S., D'Alpaos, A., & Lanzoni, S. (2021). Astronomic link to anomalously high mean sea level in the northern Adriatic Sea. Estuarine, Coastal and Shelf Science, 257(February), 107418. https://doi.org/10.1016/j.ecss.2021.107418

Van Ledden, M., Wang, Z. B., Winterwerp, H., & De Vriend, H. (2004). Sand-mud morphodynamics in a short tidal basin. Ocean Dynamics, 54(3–4), 385–391. https://doi.org/10.1007/s10236-003-0050-y

van Rijn, L. C. (1984). Sediment Transport. Part II: Suspended load transport. Journal of Hydraulic Engineering, 110(11), 1613–1641.

Van Rooijen, A., Van Thiel de Vries, J., McCall, R., Van Dongeren, A., Roelvink, J., Reniers, A., 2015. Modeling of wave attenuation by vegetation with xbeach, in: E-proceedings 36th IAHR World Congress, Citeseer. pp. 1–7

Viero, D. Pietro, & Defina, A. (2016). Water age, exposure time, and local flushing time in semi-enclosed, tidal basins with negligible freshwater inflow. Journal of Marine Systems, 156, 16–29. https://doi.org/10.1016/j.jmarsys.2015.11.006

Young, I. R., & Verhagen, L. A. (1996). The growth of fetch limited waves in water of finite depth. Part 1. Total energy and peak frequency. Coastal Engineering, 29(1–2), 47–78. https://doi.org/10.1016/S0378-3839(96)00006-3

WW3DG. (2019). The WAVEWATCH III® Development Group, 2019: User manual and system documentation of WAVEWATCH III® version 6.07. Tech. Note 333. College Park, MD, USA: NOAA/NWS/NCEP/MMAB.

Zanchettin, D., Bruni, S., Raicich, F., Lionello, P., Adloff, F., Androsov, A., et al. (2021). Sea-level rise in Venice: Historic and future trends (review article). Natural Hazards and Earth System Sciences, 21(8), 2643–2678. https://doi.org/10.5194/nhess-21-2643-2021

Zarzuelo, C., López-Ruiz, A., D'Alpaos, A., Carniello, L., & Ortega-Sánchez, M. (2018). Assessing the morphodynamic response of human-altered tidal embayments. Geomorphology, 320, 127–141. https://doi.org/10.1016/j.geomorph.2018.08.014

Zecchin, M., Baradello, L., Brancolini, G., Donda, F., Rizzetto, F., & Tosi, L. (2008). Sequence stratigraphy based on high-resolution seismic profiles in the late Pleistocene and Holocene deposits of the Venice area. Marine Geology, 253(3–4), 185–198. https://doi.org/10.1016/j.margeo.2008.05.010